We are IntechOpen, the world's leading publisher of Open Access books Built by scientists, for scientists

4,800
Open access books available

122,000
International authors and editors

135M
Downloads

Our authors are among the

154
Countries delivered to

TOP 1%
most cited scientists

12.2%
Contributors from top 500 universities

WEB OF SCIENCE™

Selection of our books indexed in the Book Citation Index in Web of Science™ Core Collection (BKCI)

Interested in publishing with us?
Contact book.department@intechopen.com

Numbers displayed above are based on latest data collected.
For more information visit www.intechopen.com

7

Applied Radiologic Science in the Treatment of Pain: Interventional Pain Medicine

Kevin L. Wininger[1,2]
[1]*Orthopaedic & Spine Center, Columbus, Ohio*
[2]*Otterbein University, Westerville, Ohio*
USA

1. Introduction

Accompanied by the work from innovative physician researchers and biomedical engineers who introduced new techniques and devices to expand armamentariums in interventional pain medicine in the 1990s and 2000s, the first decade of the 21st century resulted in a significant rise in the number of interventional procedures performed for pain management. For example, data from the Centers for Medicare and Medicaid Services shows a 518% increase from 1997 through 2006 in the Medicare population receiving spinal cord stimulation therapy (Manchikanti et al., 2009). Other examples include the efforts to design radiofrequency probes to target the sacroiliac joint and subsequently denervate this relatively complex but biomechanically unique structure with as little local tissue trauma as possible (Wininger, 2010); or the application of novel neuromodulation techniques to treat challenging cases of headache (Deshpande & Wininger, 2011).

The use of ionizing radiation for image construction (x-ray imaging) continues to be the standard in image guidance at many interventional pain medicine centers. Hence, the competent use of x-radiation not only benefits patients as well as physicians and ancillary staff in close proximity to the patient at the time of treatment—but from a health physics point of view also yields benefits for the general population given that recent evidence points to an overall increase in the use of radiation in medicine (Fazel et al., 2009; U.S. National Academy of Sciences, 2006). As of 2007, for example, medical sources of radiation represented the primary source of radiation exposure in the United States. Comparatively speaking, natural sources accounted for 3.0 mSv of the total dose, whereas medical sources accounted for 3.2 mSv (which was 5.9 times higher when compared to benchmark figures from 1980). The increase was primarily due to increased use of computed tomography (CT) and nuclear medicine studies. Note that medical sources were delineated as follows: 1.5 mSv from CT, 0.7 mSv from nuclear medicine, 0.6 mSv from radiography, and 0.4 mSv from interventional radiology (Johnston et al., 2011).

This chapter is intended to serve as a reference to help guide interventional pain physicians in their decision-making process concerning radiation risk management. In this context, the subject matter goes beyond the traditional emphasis placed solely on the cardinal rules of radiation safety (i.e., time, distance, and shielding) to render a systematic review of the different interventional imaging modalities used in the treatment of pain, namely fluoroscopy, CT, and ultrasound. Notably, we will center our discussion on the so-called

"imaging (or 'viewing') chain" of each modality, and thus the issues surrounding image quality and signal processing relative to radiation exposure (or the lack thereof in the case of ultrasound imaging). Moreover, to develop a fundamental understanding of signal processing, key physical and mathematical concepts will be explored.

While this chapter is well-motivated allowing each section to stand alone, the subject matter is presented in such a way to promote continuity from one section to the next. We begin by focusing on fluoroscopic guidance; here analysis has been included to help establish benchmark radiation exposure for spinal cord stimulation procedures as first reported by Wininger et al. (2010). We then look closely at interventional approaches in pain medicine that utilize CT. Throughout these sections, ways to mitigate radiation dose will be considered, including recent steps to improve the shielding afforded by radiation protection apparel. Next, we provide an overview on ultrasound-guided pain medicine; here the tradeoff between spatial resolution and achievable depth of imaging is highlighted. Finally, future directions in image guidance for pain management will be surveyed, including non-ionizing radiation emitting modalities such as ultrasound imaging beyond regional anesthesia and interventional magnetic resonance imaging.

2. Fluoroscopy and interventional pain medicine

2.1 The fluoroscopic imaging chain

Overall radiographic quality is based on two principal properties, photographic quality (i.e., visibility of detail) and geometric quality (i.e., sharpness of detail) (Carlton & Adler, 2006; Bushong, 2004). Photographic quality is determined by density and contrast, whereas geometric quality is governed by recorded detail (i.e., resolution) and image distortion. In fluoroscopic image acquisition, the term "density" (a term derived from static film-based radiography) is replaced by the term "brightness" to be congruent with the language used to describe the visibility of images on a display monitor. The notion of an imaging chain makes reference to highly integrated instrumentation (together with the patient), regardless of the modality of interest. The fluoroscopic imaging chain denotes the x-ray generator, x-ray tube, collimator and filtration, table and patient, grid, image intensifier, optical coupler, and the image viewing system (Schueler, 2000). To this end, while each link in the chain is of equal importance, an understanding of fluoroscopic image quality relative to the image intensifier will be emphasized. The image intensifier functions as a "pass-through" device by converting x-rays to light (fluorescence) and then to electrons by way of its input phosphor-screen with adjoined photocathode backing (see Figure 1). This design effectively and efficiently reduces overall radiation exposure (Wang & Blackburn, 2000), and at the same time, allows physicians to dynamically view anatomy with a relatively high degree of resolution due to the total brightness gain. It is the ability to view dynamically with excellent image resolution—that underpins the role of fluoroscopy in many of the modern disciplines of medicine.

The potential for x-rays to penetrate an object (i.e., soft tissue or bone) and create an image is related to the quality of the x-ray beam as a result of the operating kilovoltage (kV) at the x-ray tube, and may simply be referred to as the "x-ray tube intensity," "tube intensity," or "tube potential." The amount of x-rays produced is related to tube current (in milliamperage (mA)) and time (in seconds (s)). Whereas the operator presets these factors in static film-based radiography, producing kilovoltage peak (kVp) and milliamperage seconds (mAs) upon exposure, this is not commonplace in fluoroscopic imaging due to automatic brightness control and real-time intended-use. Automatic brightness control is a type of

automated "negative feedback" commonly set by most operators to ensure a proper amount of x-rays in order to image patients with thin to average body types. Because of its real-time imaging capability, extended exposure times are possible when operating fluoroscopy systems, and thus, the amount of tube current is substantially less compared to that used in static film-based radiography, 1 to 5 mA versus 100 to 500 mA, respectively (Carlton & Adler, 2006; Bushong, 2004). However, the physician has likely encountered degradation of recorded detail while using fluoroscopy due to a blotchy or grainy appearance that is directly related to an insufficient amount of radiation to create a uniform image (a phenomenon common to all electromagnetic imaging modalities) (Carlton & Adler, 2006). This is referred to as quantum noise or quantum mottle, as "quantum" means counted or measured. According to Carlton and Adler (2006):

> With fluoroscopy, the time factor is controlled by the length of time the eye can integrate, or accumulate, light photons from the fluoro imaging chain. Because this period is 0.2 seconds, fluoroscopy must provide sufficient photons, through mA, to avoid mottle. Quantum mottle is also a large part of video noise and is a special problem during fluoroscopy because the units operate with the minimum number of photons possible to activate the fluoro screen. The factors that influence mottle are those that affect the total number of photons arriving at the retina of the eye. This includes radiation output, beam attenuation by the subject, the conversion efficiency of the input screen, minification gain, flux gain, total brightness gain, viewing system, and the distance of the eye from the viewing system. Increasing the efficiency of any of these factors can assist in reducing quantum mottle, but the most common solution is to increase the fluoro tube mA.

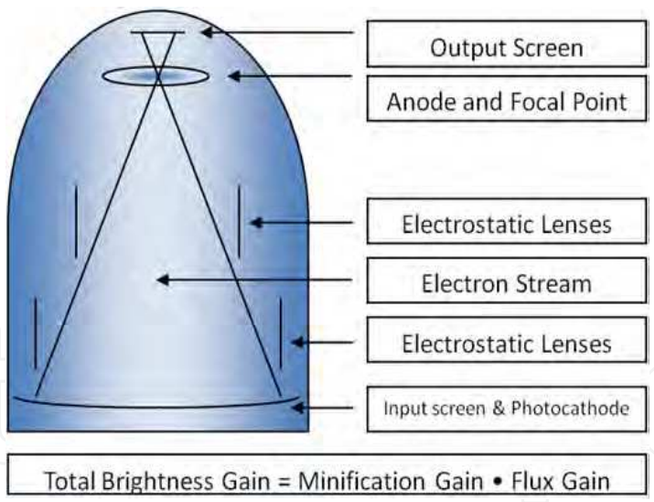

Fig. 1. Inside the image intensifier tube, x-rays photons are converted to light photons at the input screen and then to electrons at the photocathode. Flowing through the image intensifier tube the electron stream is repelled by the negatively charged electrostatic lenses and is attracted to the positively charged anode. Electrons are converted back to light at the output screen in order to proceed to the image viewing system. The output quantity of light photons is significantly greater than the input quantity of x-ray photons due to total brightness gain.

Image degradation from quantum mottle not only presents patient safety concerns due to challenges surrounding needle placement, particularly in patients with hypersthenic body

habitus, but can also be a concern to the interventional pain physician and staff members inside the fluoroscopy suite, especially when team members are standing near the patient. We turn to x-ray attenuation physics to help us better understand this (McKetty, 1998). We see that in most fluoroscopically-guided pain procedures, the primary beam is directed at bony structures (i.e., material with a large content of calcium atoms, atomic number-20, which efficiently attenuates the beam) as opposed to soft tissues (i.e., material containing more atoms of carbon, oxygen, and hydrogen, producing an effective atomic number-7.4 and thus allowing more of the beam to transmit to the image intensifier). Moreover, Table 1 lists differences in the atomic numbers and densities of matter found in the makeup of the human body. It follows that in order to compensate for the attenuated beam within the field-of-view for bony imaging compared to soft tissue imaging, radiation output ramps up either as a result of adjustments to technique factors via automatic brightness control or by means of manual technique adjustments or activation of high-fluoro/boost mode by the operator. It is also important to note that most manufacturers incorporate an increase in mA during pulsed fluoroscopy to maintain equivalent image perception (Mahesh, 2001). With this in mind, a study on perceptual comparison between pulsed and continuous fluoroscopy concluded that the average absolute differences in the equivalent-perception dose is approximately 3% (Aufrichtig et al., 1994), where the equivalent-perception dose is defined as the dose of radiation in pulsed mode needed to give the visual equivalence in continuous mode. Thus, we find, importantly, an average radiation dose savings of 22%, 38%, and 49% for pulsed-15 frames per second, pulsed-10 frames per second, and pulsed-7.5 frames per second, respectively (Aufrichtig et al., 1994).

Matter	Effective Atomic Number	Density (kg/m^3)
Air	7.78	1.29
Fat	6.46	916.
Soft Tissue	7.40	n/a
*Water	7.51	1000.
Muscle	7.64	1040.
Spongy Bone	12.31	1650.
Compact Bone	13.80	1850.
Calcium	20.00	n/a

Adapted from Johns & Cunningham, 1983, and Dowd & Tilson, 1999.
*Note: x-ray output relative to the density of water serves as a baseline measure of x-ray output in the original design and calibration of x-ray producing systems as well as many radiation dose models, and may still be used to check system standards during annual physics acceptance testing. To this point, CT systems assign the number zero to water when calculating voxel/pixel brightness values (see Figure 6, CT Numbers and Hounsfield Units).

Table 1. Differences between matter in the makeup of the human body.

2.2 The physics of fluoroscopy

2.2.1 Primary radiation

When the x-ray tube is activated, electrons are "boiled off" from the wire element (i.e., a thin filament of tungsten) to form an electron cloud (see Figure 2). The wire element is strategically located opposite from the spinning target anode as part of a built-in concavity (of which the rim is slightly more negatively charged to concentrate the electrons in the

cloud) on the cathode. The number of electrons boiled off is directly related to the tube current. Occurring nearly simultaneously with tube activation, the electrons in the electron cloud are forcefully attracted to the target anode due to the potential difference between the cathode and anode. The rate of speed and the efficiency of attraction are dependent on the potential difference across the tube. When high-speed (incident) electrons strike the target, the change in kinetic energy produces only less than 1% of x-rays, with most of the change occurring in the form of heat production (99% or greater) (Dowd & Tilson, 1999). More specifically, x-rays are generated by two processes. The first process involves the interaction of electrons with the nucleus of an atom of tungsten in which the incident electron slows down to change direction (called bremsstrahlung, or "braking radiation"). Bremsstrahlung radiation is emitted from zero to the maximum energy (operating kV). The second process is a collision of the incident electron and an outer shell electron of the tungsten atom. The collision knocks the outer shell electron out of orbit (producing characteristic radiation). Characteristic radiation is the term used to reference the fact that the x-ray energy produced is related to the binding energy between the outer shell electron and the nucleus of the target atom, and is always the same for a specific target atom (again, tungsten in the case of x-ray production in fluoroscopy) (Dowd & Tilson, 1999).

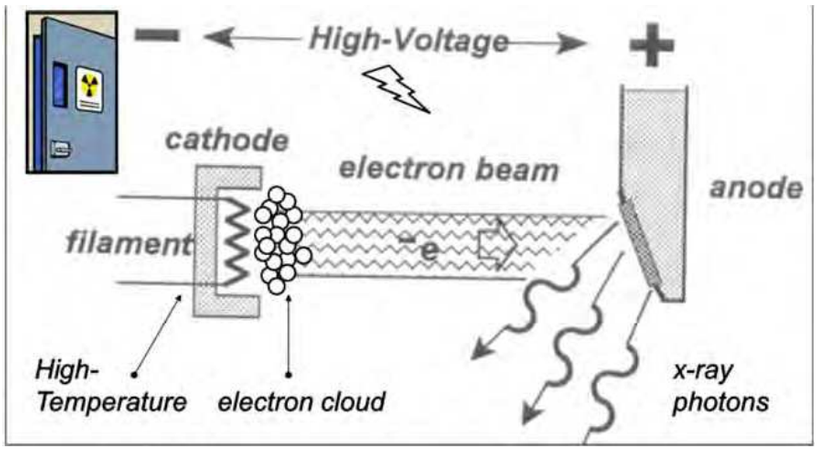

Fig. 2. A closer look inside the x-ray tube. When **tube current** is applied the filament heats up to boil off electrons into a cloud. X-rays are produced as the **tube potential** forces the incident (free) electrons to strike the target on the anode at a high-speed.

2.2.2 Secondary radiation—the patient as the point source

When x-ray photons in the primary beam pass through matter, they either pass unaltered (transmission) or undergo attenuation. Moreover, attenuated x-ray photons are either absorbed (all energy lost and the photon "dies") or scattered (some energy lost and the photon changes direction). The x-ray photons which are absorbed are primarily responsible for patient radiation exposure (via the photoelectric effect) and those photons which scatter are responsible for occupational radiation exposure (via Compton scattering). Note: when tube potential increases the photoelectric effect decreases *greatly* and the percentage of Compton interactions decreases *slightly*. (Dowd & Tilson, 1999). We will further elucidate the significance of the patient as the point source when discussing radiation risk management in fluoroscopy (or otherwise briefly stated, the occupational exposure due to secondary radiation emanating from the patient due to the interactions between the primary beam and the patient).

2.3 Fluoroscopically-guided pain medicine procedures

Nearly all interventional pain treatments and techniques evolved using fluoroscopic guidance. This was, in part, due to the capability of fluoroscopy systems to render high resolution images of bony anatomy (and adjacent tissues) to target pain generators. Today, with the versatility afforded by mobile C-arms (Tuohy et al., 1997), together with continued fidelity of the images rendered, the fluoroscope remains the principal modality for pain medicine image guidance. As a resulting consequence of this history, the literature not only contains several articles on the pros and cons of imaging techniques (for example, see Kapural and Goyle, 2007), but also contains multiple and diverse reports on radiation exposure associated with interventional pain procedures.

Notably, data collected on fluoroscopy time (the traditional metric used for clinical radiation management) serves to benchmark performance (Balter, 2006). While this parameter (fluoroscopy time) plays an essential role in the development of suitable registries to catalog radiation exposure levels according to the different pain procedures being performed, it may also be said that it is simply an awareness of this parameter by the physician that is inherent to optimization strategies in health physics (Shahabi, 1999). Table 2 presents the fluoroscopy times reported for the more common interventional pain medicine procedures using mobile multi-directional fluoroscopy systems (i.e., the conventional mobile C-arm). Other data noteworthy to collect includes: dose settings employed (operator chosen) and patient body mass. It is this additional information along with fluoroscopy time which may be used to calculate patient radiation dose received (i.e., entrance skin exposure). Table 3 shows fluoroscopy time as well as radiation dose using mobile multi-directional systems or biplanar systems for vertebral augmentation procedures.

Botwin **2001** **2002** **2003**	*Wininger **2010**	Zhou **2003**	Manchikanti **2002**	Manchikanti **2003a**	Manchikanti **2003b**	
–	–	–	13.2	8.9	12.5	Per Procedure
–	–	–	7.7	4.9	7.5	Per Patient
–	–	81.5	–	4.5	5.8	Facet Nerve Blocks
–	–	–	5.9	–	–	Cervical
–	–	–	5.5	–	–	Thoracic
–	–	–	5.7	–	–	Lumbar
–	–	50.6	–	–	7.5	Sacroiliac Joint Blocks
–	–	46.6	3.75	2.7	3.7	Epidurals
–	–	–	–	–	–	Interlaminar
12.6	–	–	–	–	–	Caudal
–	–	–	8.8	–	–	TFESI – Cervical
15.2	–	–	10.9	–	–	TFESI – Lumbar
–	–	–	12.7	–	–	Medial Branch Block
57.2	–	146.8	–	–	–	Discography
–	133.4	–	–	–	–	Spinal Cord Stimulation

*Wininger et al. also reported calculations on entrance skin exposure.

Table 2. Fluoroscopy time (in seconds) using mobile multi-directional systems.

Kallmes **2003**	Boszczyk **2006**	**Perisinakis **2004**	***Villavicencio **2005**	***Izadpanah **2009**	Thoracic Spine
522	216	609	81.3	175	Total Fluoroscopy Time
–	100	203	–	–	Total Patient *ESE*
–	32	–	–	–	*ESE* – AP Imaging
–	68	–	–	–	*ESE* – Lateral Imaging
–	–	3598	–	1245	Total DAP
–	–	2294	–	–	DAP – AP Imaging
–	–	1304	–	–	DAP – Lateral Imaging
–	–	–	–	–	Effective Dose/Minute
236	–	–	–	–	Physician Hand

**without or ***with 3D navigation in vertebroplasty or kyphoplasty procedures.
Fluoroscopy time (in seconds); patient entrance skin exposure (*ESE*) and dose area product (DAP, a calculation of stochastic risk for the patient [Vano et al., 2001]) (in centiGray); physician total and hand exposure (in microSieverts/minute).

Table 3. Radiation exposure associated with biplanar systems or multi-directional systems.

Inter-procedural variance compared to fluoroscopy times observed in Tables 2 and 3 may be attributed to differences in procedural techniques, level of experience, and/or physician preferences in imaging assistance, as well as attenuation physics relative to image quality. To illustrate this last point, we consider spinal imaging. During spinal imaging, two common challenges associated with image quality exist: 1) highly radiolucent vertebral bodies, particularly against the imaged lung field, creating excess image brightness in the region of interest, and 2) large body habitus with resultant poor image quality. In the former, tight collimation with the paired leaves shutters drawn close to the spine and continuous-mode imaging may help compensate for poor contrast resolution due to the vertebral bodies lacking enough cortical bone density to effectively attenuate the beam (i.e., low beam attenuation) (Johns & Cunningham, 1983). Subsequently, overriding automatic brightness control by manually ramping down tube current (mA) during tightly collimated bony imaging can help improve image resolution, especially for extremely radiolucent vertebral bodies. Alternatively, a manual adjustment to monitor/display window contrast may effectively improve image quality. To compensate for poor image quality secondary to large body habitus (i.e., a highly attenuated beam with resultant image granularity), it too may be necessary to operate the fluoroscope in continuous mode to increase the overall radiation at the image intensifier rather than disengaging the low dose feature. This strategy may improve image contrast while limiting patient exposure if a "manual beam on/off" operator technique is used, e.g., while panning or moving the C-arm between anteroposterior/oblique positioning to keep region of interest in the field of view.

2.4 Radiation risk management/safety

In recent years the assessment of radiation dose has received increased scrutiny; notably, the evaluation of deterministic effects, for which the severity of effects will vary according to the dose received and for which dose thresholds usually exist (e.g., radiation induced skin injuries) (Balter, 2006 & 2008). Moreover, dose assessment has seemingly evolved from an academic enterprise to a clinical endeavour. Direct influence on clinical practice is appreciated by The Joint Commission's recent decision to add unexpectedly prolonged fluoroscopic exposure to its list of reviewable sentinel events, as well as their suggestion to

follow-up qualifying events with a period of over six-months to one-year to monitor cumulative skin dose (The Joint Commission, n.d.). While fluoroscopy time alone provides inadequate skin dose estimates (Balter, 2006; Balter, 2008), the evaluation of incident air kerma (x-ray exposure to the skin, previously referred to as entrance skin exposure) is possible by simplistic modeling (Balter, 2008; American Association of Physicists in Medicine (AAPM), 2001; Bushong, 2004).

In part with its approach to minimally invasive treatments and therapeutic procedures, interventional medicine is the one branch of medicine which, in its practice, is riddled with concepts that stem from physics. It may be further stated that physicians, even interventionally-trained physicians, may feel as though they are not able to translate applicable literature into everyday practice without possessing a doctorate in the physical sciences. For example, radiation dose models can be complicated as there exists many nuances when talking about dose, and the units of measure are not intuitive. However, both radiation safety and radiation protection are fundamental considerations for the interventional pain physician, and are equally paramount responsibilities in the interventional pain practice. In the view of the author, physicians who utilize fluoroscopic guidance will find that keeping radiation exposure, and therefore radiation dose, as low as reasonably achievable (given the acronym ALARA) is a challenge that is not insurmountable. This goal is achieved by exploitation of the principles unique to image acquisition in fluoroscopy, together with radiologic physics and applied radiobiology (Dowd & Tilson, 1999), and a suitable quality assurance program. Thus, by first laying out the conversion between the basic units of measure in radiation physics,

$$1\,R \approx 1\,rad = 10\,mGy = 10\,mSv$$

this section will strive to provide the interventional pain physician with information on radiation risk management which may be readily acted on and implemented.

Entrance skin exposure is the radiation exposure to the skin measured in Roentgen (R) or milliRoentgen (mR) at the point of skin entrance for the nominal patient (i.e., 30 cm from the image intensifier). The measurement is made without the contributions from scatter radiation. In compliance with physics acceptance testing, the fluoroscopic tube potentials (kVp) under automatic brightness control should operate at/or between 70 and 90 kVp with 3.8 cm of aluminum (~15 cm of water or acrylic plastic) attenuation material. This produces measured fluoroscopic exposure rates in the range of 1.0 to 4.0 R/minute for all magnification modes (fields of view) for continuous mode in the normal dose setting (AAPM, 2001; Bushong, 2004). The lower portion of the exposure range accounts for the largest field of view (least magnification), and the upper portion of the exposure range accounts for the smallest field of view (most magnification). The name of the quantity which corresponds to entrance skin exposure and which is recognized by the International Commission on Radiation Units and Measurements is incident air kerma (Balter, 2008), and the unit of measurement is milligray (mGy). (Note: 1 R = 1 Roentgen = 2.58×10^{-4} coulombs/kg-m of air at standard temperature and pressure, and 1 R = 8.76 mGy [milligray].)

The dedicated use of the low dose setting (which provides 40% or more dose reduction compared to the normal dose setting, Smiddy et al., 1996; Davies et al., 2006), when paired with pulsed fluoroscopy (which provides 50% dose reduction at 7.5 frames per second, Aufrichtig et al., 1994) promotes optimal radiation risk management. This impact is best observed by a closer inspection of the work by Wininger et al. (2010) on radiation exposure in spinal cord stimulation [trialing] procedures. The authors point out that although pulsed

fluoroscopy was utilized differently during cases #3 and #43, the fluoroscopy time for each case was recorded as 198.9 seconds. Analysis between actual settings used and hypothetical use variances for the low dose setting and the pulsed mode feature, based on simplistic modeling, illustrated how fluoroscopy time alone may lead to inadequate skin dose assessments. In other words, analysis of incident air kerma derived from the actual settings revealed that case #43 incurred 39.4% more skin exposure than case #3. Hypothetically, if neither the low dose feature nor pulsed fluoroscopy had been utilized, the resultant incident air kerma (i.e., 38.7 mGy) would have approximated the actual estimates derived for fluoroscopy times greater than 300 seconds (i.e., approximately double) for this procedure (i.e., 25.7–43.7 mGy). However, because the earliest deterministic threshold is 2.0 Gy, the level associated with transient erythema (Geleijns & Wondergem, 2005), research indicates that induction of deterministic insults (such as skin injuries) is highly unlikely during interventional pain medicine procedures. *Rather, in interventional pain medicine, the prime objective is to safeguard to the degree possible (i.e., ALARA) against low doses of x-radiation (U.S. National Academy of Sciences, 2006; Little et al., 2009).*

With respect to quality assurance programs for fluoroscopy systems, it is important to address mechanical and electrical safety in addition to radiation safety and image quality. Moreover, such programs are particularly important for mobile systems due to the various uses and locations in which these units are intended to perform. Given that mobile units are often the more commonly utilized systems in pain management applications, a quality assurance protocol is essential. However, due to differences between mobile systems from the various manufacturers, as well the different regulations overseeing radiologic licensure in the various jurisdictions the reader finds him- or herself in, an outline of such program is beyond the scope of this chapter. The reader is, therefore, referred to Tuohy et al. (1997) who tackled these issues and made several key recommendations.

Reports on occupational incurred dose from scatter radiation are typically based on radiation exposure to standardized phantoms, thus representing the symmetrical ideal "small lumbar" spine. This methodology, however, may potentially underestimate the amount of occupational radiation exposure since body habitus does not always lend itself to symmetry and body size varies from patient to patient. Hence, Whitworth (n.d.) performed scatter radiation vector analysis on the lumbar spines of five cadavers to better parallel the general experience of the interventional pain physician and those team members inside the fluoroscopy suite. The study employed an OEC 9800 mobile C-arm with automatic brightness control engaged. Radiation exposure was recorded using Geiger Mueller techniques (measurements are shown in Table 4).

OEC 9800	mrem/hour	kV	mA
High Level/Boost Fluoro	204	71	3.9
Normal Dose	111	70	2.2
Low Dose	56	72	0.76
Low Dose + Collimation	15	74	0.82
Pulsed-8 frames per second	7	76	0.86

Meter set at 17 inches above the floor and 12 inches lateral to the image intensifier.

Table 4. Scatter radiation measurements: imaging the lumbar spine of a cadaver with 21.5 body mass index.

Four important concepts were drawn from the resulting data set, as follows:

- Scatter radiation is exponential with increasing kilovoltage (kV) and linear with increasing mA;
- Collimation reduces scatter radiation by 50% or more;
- Use of low dose reduces scatter radiation by 50-75%; use of pulsed mode reduces scatter radiation by 65-90%; and
- Scatter radiation drops 50% every 6 inches away from the image intensifier.

It is interesting to pair the data set obtained by Whitworth with a law in radiophysics which aptly describes the phenomenon of scatter radiation in a meaningful way: as kilovoltage increases the photoelectric effect decreases *greatly* and the percentage of Compton interactions decreases *slightly*. Thus, Whitworth actually observed the following. As tube potential (kVp) increases, fewer x-rays interact with tissue, and therefore less scatter is created. However, the scatter that is created has higher energy and is more likely to reach the image intensifier [or nearby dosimeter(s)] than to interact with the patient's body. This makes increased kVp a radiation protection tool that must be counterbalanced with image concerns (Dowd & Tilson, 1999). See Table 5.

Tube Potential Kilovoltage (kVp)	**Secondary Radiation** (The Patient as the Point Source)		**Total Number of Interactions in 1mm Tissue**
	Total Number of Photoelectric Effects	Total Number of Compton Scatter/ Coherent Interactions	
50	500 (50%)	500 (50%)	1000
90	165 (33%)	335 (67%)	500

Adapted from Dowd & Tilson, 1999.

Table 5. Effects of x-ray tube potential (kilovoltage) on secondary radiation generated.

In many interventional pain suites, "lead aprons" are the principal shield for radiation protection of personnel. In addition, it should be noted that a table skirt substantially decreases occupational radiation levels—since the majority of scatter radiation is produced under the fluoroscopy table (for fluoroscopes/C-arms with under-table x-ray tubes) in the form of backscatter. Thus, significant reduction to scatter radiation is gained from the combined pair, as each scattering incidence results in x-radiation energy levels of only 1/1000 of that prior to the episode (Dowd & Tilson, 1999). Moreover, largely as a consequence of complaints of back pain over time from the wearers of lead aprons (Christodoulou et al., 2003), lead equivalent aprons became the apron-of-choice among interventionalists, and recently, "lead free" aprons have emerged in the marketplace. Such alternative materials include tin, iodine, barium, and antimony, or any combination thereof. Such "lead free" alternatives offer significant weight reduction, compared to primarily-leaded aprons, and equivalent radiation protection (Finnerty, 2005) (see Table 6). As part of an occupation radiation safety program, it is suggested that the reader ensure annual inspections of aprons are performed and rejection criteria established. Practical rejection criteria have been offered by Stam and Pillay (2008).

It is know that the dominant hand of the interventionalist receives the highest dose of radiation. It is interesting to note that a new type of sterilizable, radiation protection glove (primarily composed of tungsten) was recently tested among surgeons during a variety of cases, including micro-discectomy (Back et al., 2004). In terms of radiation protection, results revealed that the glove was superior to all other gloves in the marketplace, attenuating 90% of x-rays (see Table 6), and radiation dose to the dominant hand was reduced to less than the dose received by the non-dominant hand.

Aprons (0.25 mm)		**Aprons (0.50 mm)**			
Pure lead	Lead equivalent	Pure lead	Lead equivalent	"Lead-free"	
Attenuation at 70 kVp					
95%	92% 89-95%	99%	98-99%	n/a 98.1-98.3%	Mean Range
Transmission at 70 kVp					
	8% 5-11%		1% 1-2%		Mean Range
Attenuation at 100 kVp					
85%	83% 79-87%	95%	95% 93-96%	n/a 93.2-93.9%	Mean Range
Transmission at 100 kVp					
	17% 13-31%		5% 4-7%		Mean Range
Gloves – supplier or *type, and quoted decrease at 80 kVp					
*Tungsten		Henleys Medical (3 STAR)	Henleys Medical (2 STAR)	Henleys Medical (1 STAR)	F&L Medical Products Co.
90%		65%	57%	32%	25%

Adapted from Back et al., 2005; Christodoulou et al., 2003; and Clasper & Pinks, 1995.

Table 6. Radiation protection apparel.

Risks of cataract development due to radiation exposure to the eyes have been investigated in interventionalists, with no conclusive evidence to date. However, the use of lead-based glasses is advocated, especially when the risk of "rescatter" (radiation which emanates from within the interventionalist's head, or so-called tertiary exposure) is considered (Cousin et al. 1987). As pointed out in a review on exposure risks of interventional pain physicians, studies demonstrate a decrease in transmission rates of 70-90% with appropriate eyewear ("lead" glasses) (Fish et al., 2011). Moreover, because it is the patient that is the point source of occupational radiation risk coupled with the proximity of the interventional pain physician to the patient, positioning the monitor to require the interventionalist to look 90° (from the patient) with eyewear with side shields could further help reduce eye exposure. As stated by Fish et al. (2011), "…It is extremely vital for the interventionalist to be

cognizant of his/her surroundings. This reiterates the importance of increasing the distance between the physician and the source of the radiation, it also emphasizes decreasing the amount of exposure time, which can both drastically reduce unnecessary radiation via scatter."

2.5 Special report: Radiation exposure during spinal cord stimulation mapping: A new data set

Summary of Background Data: The increase in exposure to low-dose radiation from the growing use of medical imaging has raised concerns about cumulative dose among the general population (Fazel et al., 2009; U.S. National Academy of Sciences, 2006; Little et al., 2009), and accordingly, dose assessment has received increased scrutiny (Balter, 2008). Conversely, unique among implantable devices, some spinal cord stimulation systems utilize integrated technology to perform "electronic fluoroscopy" to assess device orientation (i.e., the leads) without irradiation (Kosek et al., 2006). Recently, however, a first look at radiation exposure from spinal cord stimulation [trialing] procedures was published to help benchmark radiation exposure reference levels for this procedure (Wininger et al., 2010). Although estimated exposure was negligible, data on patient size was unavailable and the source-to-skin distance (SSD) was not taken into account due to simplistic modeling.

Objective: To address the aforementioned limitations, radiation exposure was reexamined by the author for a new patient population.

Methods: 106 dual parallel lead spinal cord stimulation trialing procedures [using either multiple-independent current-controlled systems or constant-voltage systems] in the non-university, outpatient setting, from October 2008 to October 2009, were studied prospectively. Body mass index (BMI) measurements were retrieved. The *fluoroscopy system automatically tabulated total fluoro-time (in seconds) per case, and partitioned the absolute time- and the percentage of time allocated to- pulsed and continuous-mode imaging. High dose fluoroscopy, or "boost" mode, was not used. A study specific ‡personal dosimeter was worn by the physician. For the dose model, radiation output was measured with a §dosimeter/ion chamber located 30 cm from the image intensifier, along the central axis of an anteroposterior projected beam, and calculated based on the following equation.

$$ESE_{pat} = ESE_{pha} \bullet \left[\frac{O_{pha}}{O_{pat}} \bullet \left(\frac{SSD_{pat}}{SSD_{pha}}\right)^2\right] \bullet t_{flu}$$

Where ESE_{pat} and ESE_{pha} are skin exposure to the patient and †phantom; O_{pha} and O_{pat} are radiation output for phantom and patient exposure (in Röentgens); SSD_{pat} and SSD_{pha} are the distances from the x-ray source to the skin for the patient and phantom; and t_{flu} is fluoro-time (converted to minutes). Note: incident air kerma is measured in milligray (mGy) and is converted from ESE_{pat} by applying a factor of 8.76 mGy to 1 Röentgen. Incident air kerma estimates were stratified according to SSD and low dose mode engaged/disengaged.

Results:

Total fluoroscopy time:

Mean: 71.7 seconds
(standard deviation: 34.9 seconds)
Range: 19.5 seconds to 166.6 seconds

Percentage pulsed imaging:
Mean: 33.4%
Range: 1.80% to 75.2%
Mode: 55.4% (compiled % most frequent)
Source-to-skin distance:
Mean: not reported
Range: 43 cm to 50 cm
Body mass index:
n = 54 females
Mean: 31.54 kg/m^2
Range: 18.46-53.32 kg/m^2
n = 52 males
Mean: 29.65 kg/m^2
Range: 17.03-42.45 kg/m^2
Incident air kerma:
Mean: 8.33 mGy
Range: 1.53 mGy to 32.0 mGy
Physician dosimeter:
Whole body cumulative dose: 73 mrem

Discussion:

1. Figure 3 shows the descriptive statistical summary for fluoroscopy time. Seven outliers were identified in each data set. Notably, less variance around the median value occurred with the new data (i.e., the interquartile range was reduced by 47.4%).
2. Accounting for outliers, total fluoroscopy time was normally distributed.
   - Figure 4 compares the grouped subsets—based on one minute intervals.
3. Mean total fluoroscopy time was 46.3% less (71.7 seconds compared to 133.4 seconds). However, it is noted that outliers from the previous data set had not been removed in the reporting of that data, and thus mean total fluoroscopy time for the previous data set was artificially inflated.
4. Percentage pulsed imaging was equivalent.
5. Patient radiation exposure was reduced: 1.53—32.0 mGy compared to 1.8—43.7 mGy.
6. Patient size ranged from mildly underweight to morbidly obese according to BMI (as defined by the World Health Organization, n.d.). The mean BMI, by gender, bordered pre-obese and obese.
   - Note: trending increase in body weight among the U.S. population paired with concern about cumulative dose trends (Yanch et al., 2009; Fazel et al., 2009) underscore the need to obtain accurate reference levels on radiation exposure, as such exposure will, in general, be higher for patients with greater body mass.
7. Estimates for incident air kerma were stratified according to various SSDs, see Figure 5.

Conclusions:

Radiation exposure from spinal cord stimulation trialing procedures remains negligible despite the likelihood, as suggested here, for this therapy to be used in a patient population with a greater risk for increased irradiation based on BMI valuations.

Acknowledgements:

The author thanks Siva Gopal, PhD, Otterbein University, for his constructive instruction in descriptive statistical methods.

Footnotes:

*OEC 9800 Super-C, GE Healthcare, Salt Lake City, UT, USA.
†Phantom: 3.8 cm of aluminum.
‡Badge report, study specific: Luxel, optically stimulated luminescence dosimetry, LANDAUER, Glenwood, IL, USA.
§Radiation meter – Model 1515 with converter model 1050U and ion chamber model 10X6-6M, Radcal Co., Monrovia, CA, USA.

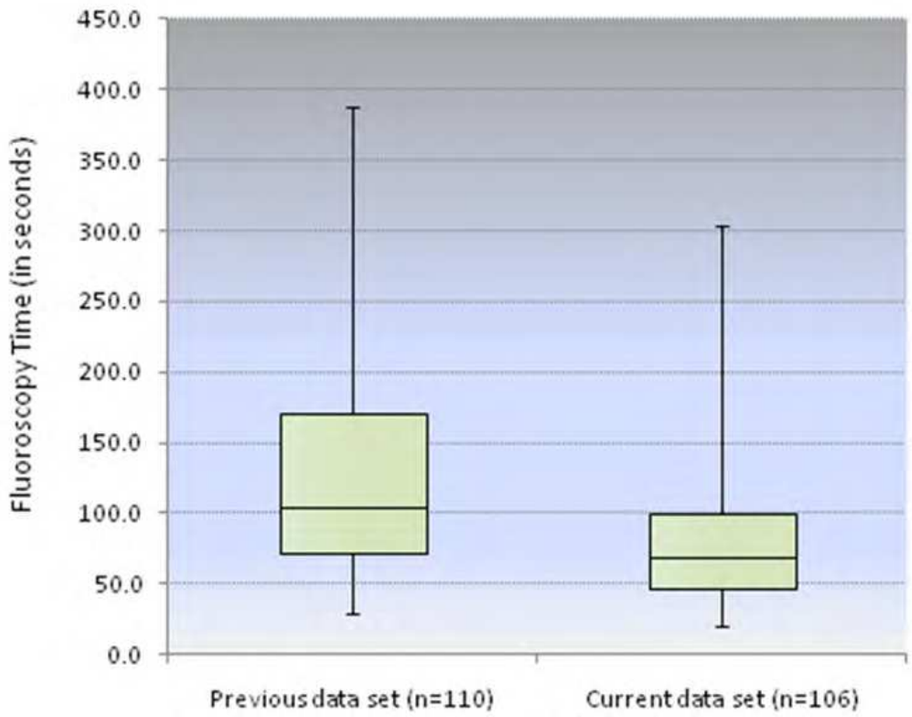

	Previous data set (n=110)	Current data set (n=106)
Interquartile Range	98.9	52.0
Lower Fence	-76.6	-30.8
Upper Fence	319.1	177.2
Outliers	321.1	208.9
	329.3	217.7
	336.2	236.3
	343.8	239.4
	373.1	294.0
	387.2	299.7
	387.4	304.0

Fig. 3. Box plots comparing previous and current fluoroscopy time data sets for spinal cord stimulation mapping procedures. Note: Because all data (both sets) were obtained from the same interventional spine team, inter- and intra- procedural variability was minimized.

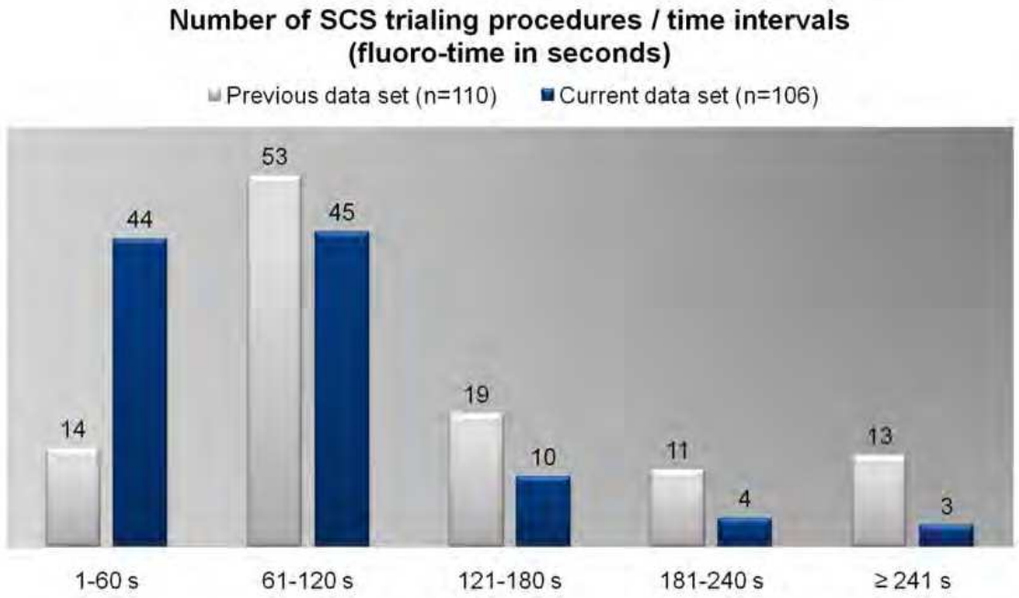

Fig. 4. Bar chart comparing the prior and new data sets with respect to fluoroscopy time during percutaneous spinal cord stimulation mapping procedures.

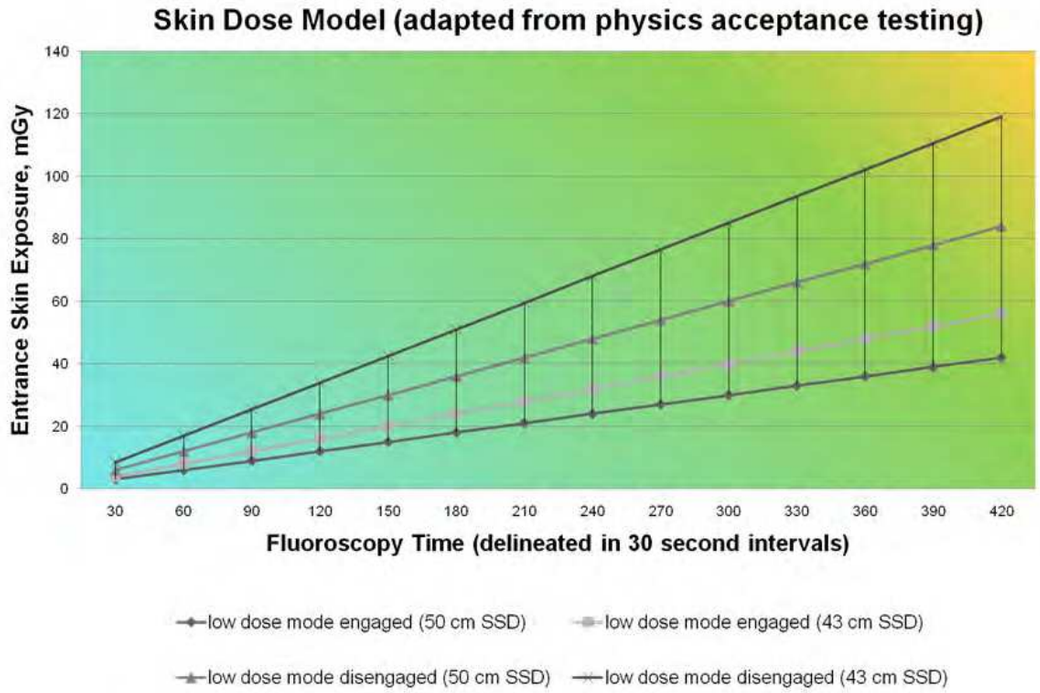

Fig. 5. ESE_{pat} to anterior chest: 50 kg. adult patient accounting for one dose reduction feature, i.e., the low dose mode, either "on" or "off" for stratified SSDs (either 43 cm or 50 cm) in percutaneous spinal cord stimulation mapping. (Note: valuations represent continuous-mode imaging, no beam collimation.)

3. Computed Tomography (CT) and interventional pain medicine

3.1 The CT imaging chain

Although the underlying physical concepts are, for the most part, the same (such as x-ray production), the CT imaging chain offers a higher level of sophistication compared to the imaging chain of fluoroscopy. This is exemplified by the application of mathematical filters selected for a desired level of image reconstruction to control signal/quantum noise to optimize image quality (Sprawls, 1992), and most commonly applied using high-pass filters to control edge artifacts. According to Barnes (1992), while the CT scanner is capable of dividing its measurement of tissue attenuation into a range of 4,096 CT numbers, the eye is not capable of distinguishing this much detail in an image. The image display of a CT scanner represents only 256 levels of gray, which must therefore be mapped onto the portion of the Hounsfield scale that is to be displayed. Adjustments called "window level" and "window width" are used to define this mapping. Selection of the window level (i.e., brightness) specifies the CT number for centering the gray scale, and choice of the window width (i.e., contrast) defines the range of CT numbers over which the gray scale is to extend. These adjustments can be thought of as defining the "slope" of the gray scale. When the gray scale is placed at a window level of 100 and the window width is set at 500, the gray scale permits display of CT numbers from -150 to +350. All CT numbers below the lower limit of the window width are displayed as black, and all those above the upper limit are displayed as white on the image (see Figure 6).

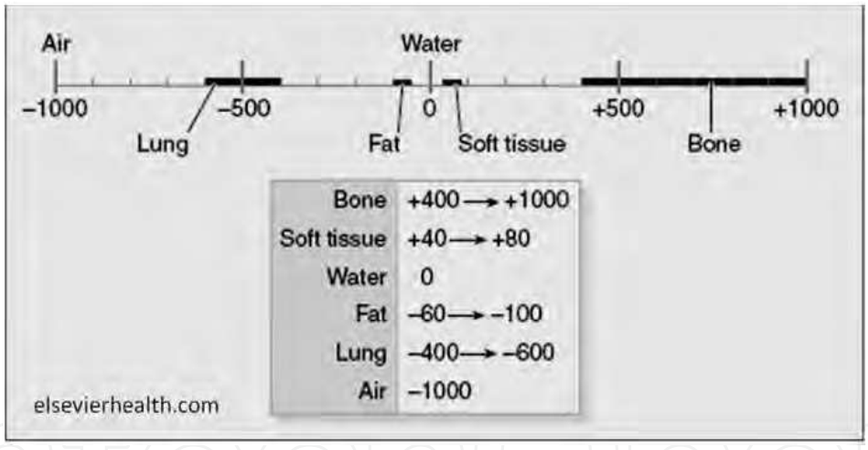

Fig. 6. CT Numbers = Hounsfield Units.

3.2 The mathematics of CT physics

The language of mathematics not only permeates all scientific study, but the very application of mathematics itself allows exploration to occur at the limits-of-discovery to find answers to questions that vex human nature. To this end, it is through a mathematical framework that physicists talk about dosimetry—with various selected examples on dosimetric methods in CT given in Table 7. Moreover, computational models for CT scanning enable testing of quality control algorithms to ultimately help reduce overexposure errors (Ferreira et al., 2010). This section will serve as a mathematical primer to highlight the physics behind image acquisition/signal processing of CT scanning to allow interventional pain physicians to gain deeper insight into this modality, and through this appreciation, demystify the process of CT imaging.

First Author	Title of Article	Citation: Journal Year;Volume:Page	
Balter	Why (Continue to) Study Physics?	Radiographics	1992;12:609
Rothenberg	Radiation Dose in CT	Radiographics	1992;12:1225
McNitt-Gray	Topics in CT: Radiation Dose in CT?	Radiographics	2002;22:1541
Bauhs	CT Dosimetry: Comparison of Measurement Techniques and Devices	Radiographics	2008;28:245
Huda	Converting Dose-Length Products to Effective Dose at CT	Radiology	2008;248:995

Table 7. Select references on the physics of CT appearing in the journals of the Radiological Society of North America.

Although the subject matter on this topic is diverse, no truly rigorous mathematical justification of a tomographic algorithm exists (Shepp & Kruskal, 1978). For this reason a generalized derivation (that of inverting the Radon transform, as this is the widely accepted technique to describe how we recapture the information lost to attenuated x-ray photons) will be described in plain mathematical language. In addition, where noted, Wolfram *Mathematica*—the online computational engine, Wolfram|Alpha™—was used to plot the traditional representative line equations of the x-ray photons. It is also important to note that in order to simplify the derivation the following three constraints will be made. First, we will ignore the playoff between Cartesian and polar coordinate representations, i.e., the 2-dimensional xy-plane versus spherical or circular symmetry. Second, we will not account for adjustments in the derivation for cone beam and/or fan-beam CT constructs due to their mathematical complexities (Note: the fan-beam third generation CT scanner, see Figure 7, is the most commonly utilized type of scanner.) Finally, discrete numerical analysis will not be

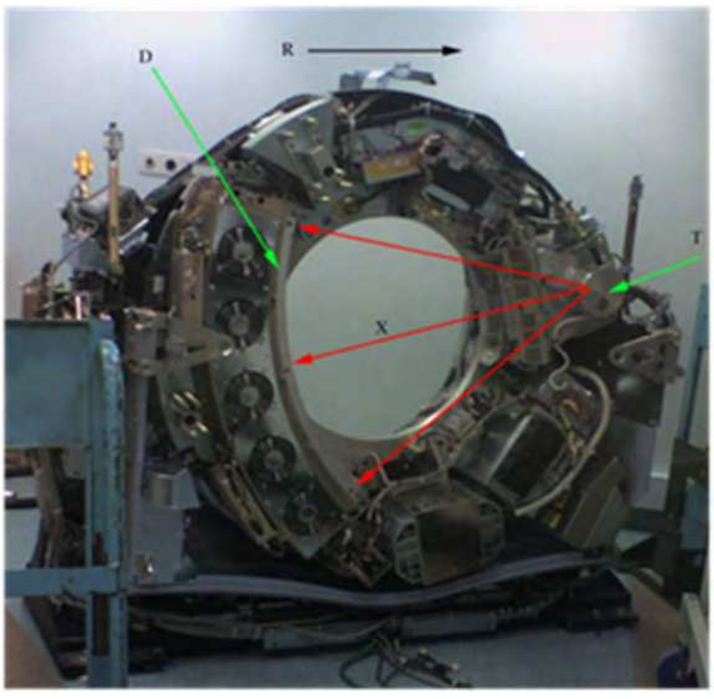

Fig. 7. Third generation "fan-beam" CT scanner.

addressed. To this end, the steps necessary to invert the Radon transform with respect to the parallel beam model (and thus most enthusiastically applicable to first and second generation CT scanners will constitute the balance of this section. It is the hope that such insight will complement the physician's knowledge-base when carrying out CT-guided pain procedures.

The set up

The underlying theme in this mathematical application is a signal processing challenge, and the set up for the analysis is straightforward. We have a 2-dimensional slice of a region of variable density (the patient), and the goal as applied to CT scanning is to reconstruct the resulting x-ray signal (the image) after repeatedly passing x-rays through the region at different angles of initial projection (the CT gantry). More concisely stated, we are measuring the resultant signal at different trajectory lines by accumulating (integrating) the signal after projecting x-ray photons through the region. Hence, the approach reconstructs the densities of the materials interacting with the x-ray photons (Johns & Cunningham, 1983), to ultimately assign density values according to the Hounsfield unit scale of CT numbers for data acquisition/image processing (Jackson & Thomas, 2004). Such modeling serves as an engineering template for trouble-shooting in the event of errors, such as equipment failure or computer algorithm failures, which may lead to radiation overdose of the patient.

Given that the approach resolves signal processing by means of calculating line integrals to recover the intensity of the x-ray signal (i.e., capture the data lost to attenuated or scattered x-rays), a comparison may be made to the inverse square law which estimates beam intensity from known initial conditions, the intensity of- and distance from- the beam (Carlton & Adler, 2006). However, the comparison is rudimentary at best because the central and interesting feature of the model applicable here, i.e., the Radon transform and its inverse, lies in the fact that we are *strictly* calculating the intensity of the exit/secondary beam based *solely* on a known intensity of the primary beam.

It is important to understand that the Radon transform refers to a special case of the Fourier transform; and the Fourier transform is a limiting case of the Fourier series (Boyce & DiPrima, 2005; Bracewell, 1986). This means whereas a Fourier series is the mathematical instrument used when evaluating periodic phenomena (Boyce & DiPrima, 2005), a Fourier transform is reserved for the study of phenomena that is nonperiodic (Bracewell, 1986). Thus, the choice of the application of a "transform" is an intuitively simple decision, given that x-ray photons in the exit beam strike the image receptor in burst-like impulses that are mostly nonperiodic rather than periodic in fashion. In mathematical terms, burst-like physical phenomena that are almost periodic are known as line impulses. *The concept of the line impulse will be a key point expanded upon below.*

The derivation of the mathematical model can be relatively easy to follow since the steps involved are pragmatic to imaging tasks carried out in the CT suite. We begin by a detailed inspection of representative x-ray trajectories relative to the CT gantry (i.e., the family of parallel lines), and then compare the suitability of two different proposed coordinate systems for the model.

Lines/family of lines

Refer to Figure 8 for a depiction of the CT gantry with the x-ray beam drawn as a family of parallel lines though the region. Each representative x-ray trajectory (i.e., the parallel lines) can be written in the slope-intercept form of a line.

$$y = mx + b \qquad -\infty < b < \infty \ , \qquad 0 \leq m < \infty$$

In this form, the coordinates of the lines in the xy-plane are the points (m,b), "m" the slope of the line and "b" the y-intercept. However, this coordinate system breaks down as "m" and "b" vary because the formula is not valid for vertical lines, such that a vertical slope is not defined (Larson et al., 2007). Therefore, a more suitable coordinate system is required to parameterize a line (and all families of parallel lines), and therefore, it is interesting to look at what a family of parallel lines may have in common (see Figure 9).

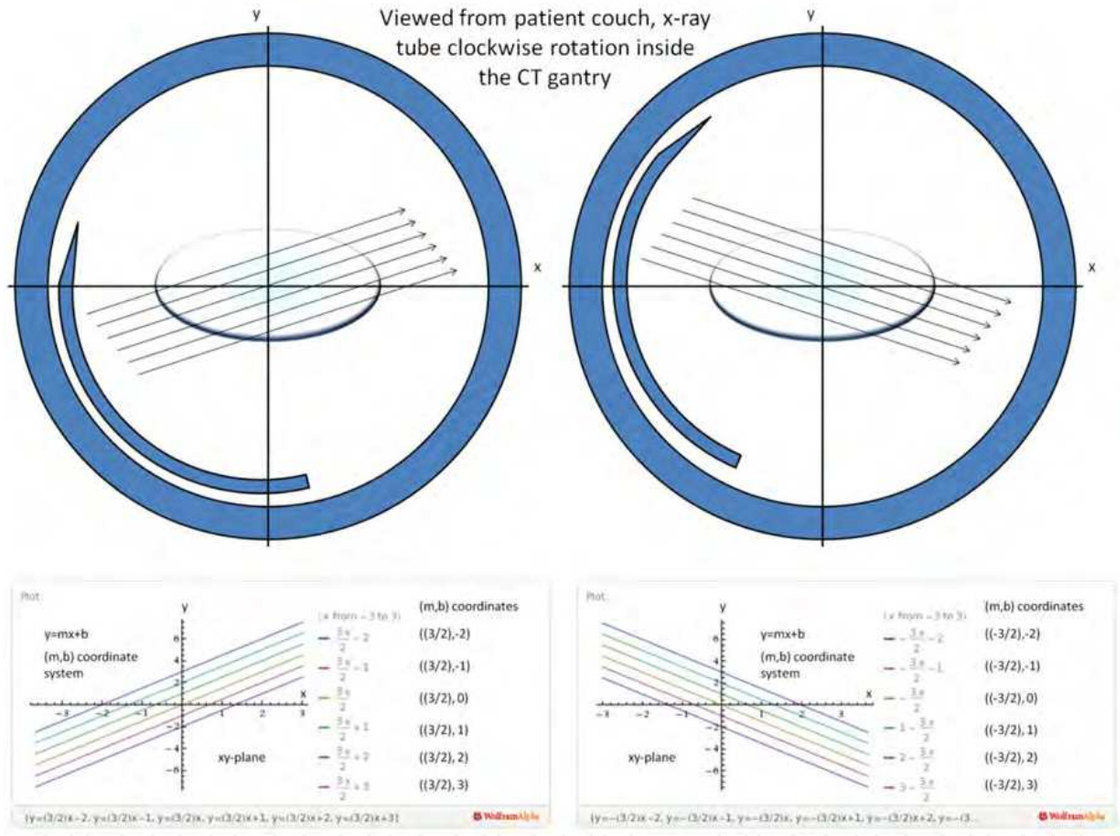

Fig. 8. (Top left) Gantry of CT scanner showing trajectories of x-rays [long arrows] emitted as lines/family of parallel lines. (Top right) Illustrated clockwise rotation of the x-ray tube inside the gantry. (Bottom left/right) Representative, corresponding line equations written in the slope-intercept form y=mx+b in the xy-plane. The (m,b) coordinates are given by the line equations.

Referring to Figure 9, one such identified commonality is that each line has the same angle to the horizontal axis, the x_1-axis. Thus, we will call this angle, the angle φ (phi). Specifically, it is the normal vectors of these lines that have the same angle to the x_1-axis. However, to better identify locations of lines, we need more than just the angle to the x_1-axis. To single-out a line we look at its distance ρ (rho) from the line passing through the origin (see Figure 9). Thus, with these parameters, the distance ρ (rho) and the angle φ (phi), we have successfully established an unambiguous coordinate system that is not flawed by the non-

existence issue of a vertical slope. The *Cartesian equation of the line for the model*, is now specified by a given coordinate pair (ρ,φ) in the form:

$$\boldsymbol{x} \cdot \boldsymbol{n} = x_1 \cos\varphi + x_2 \sin\varphi = \rho$$

where both **x** and **n** are vectors, each defined in the following way, **x**=‹x_1,x_2› and **n**=‹cos(φ),sin(φ)›, and the line equation is derived by vector multiplication, in this case by using the dot product method, where it is said that **x** is dotted with **n**.

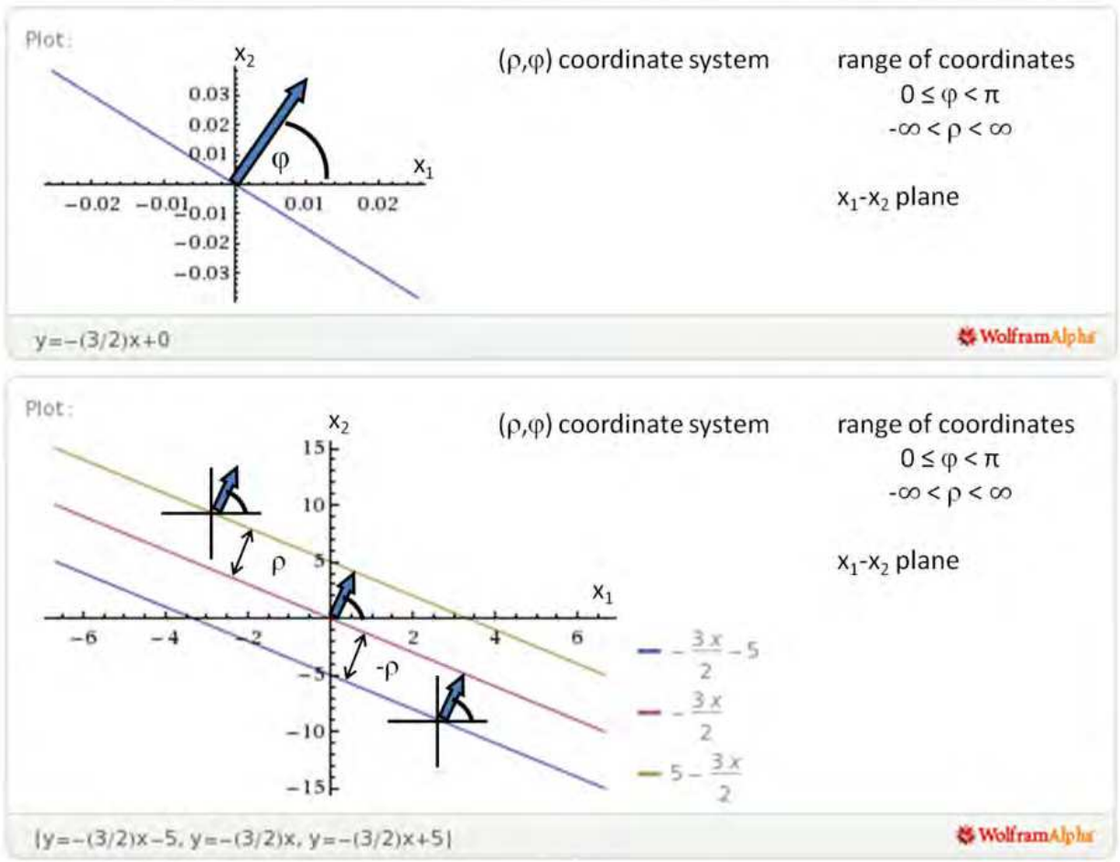

Fig. 9. A better-suited coordinate system (ρ,φ) for the model. (Top panel) Arrow demonstrating the unit normal vector associated with the line passing through the origin, and oriented with an angle phi (φ) to the x_1-axis in the x_1-x_2 plane. (Bottom panel) A family of 3-parallel lines and their unit normal vectors [arbitrarily placed on the lines] showing signed distances rho (ρ) from the origin [double ended arrows]. By convention, distances are positive [i.e., positive rho (ρ)] when measured *in the direction of the normal vector from the line passing through the origin to associated parallel lines*. In a similar fashion, distances are negative [i.e., negative rho (-ρ)] when measured *from the line passing through the origin to parallel lines spatially existing opposite to the direction established for the normal vector*. Rho (ρ) is zero at the line passing through the origin. (Note: the unit normal vectors are not drawn to scale, and when compared to Figure 8, the xy-plane has been renamed the x_1-x_2 plane.)

Line impulse

Accordingly, it is necessary to account for the nonperiodic nature of the signal concentrated along each trajectory taken by the x-ray photons, and this is accomplished by considering the line impulse (Bracewell, 1986). The line impulse describes the physical phenomena of x-ray photons striking the image receptor in the CT gantry. To define the line impulse mathematically, we first need to set the *Cartesian equation of the line for the model* to zero as shown.

$$\rho = x_1 \cos\varphi + x_2 \sin\varphi \xrightarrow[set\ to\ zero]{} \rho - x_1 \cos\varphi - x_2 \sin\varphi = 0$$

The resultant equation, specifically the left hand side of the new equation above, then becomes a function of delta, denoted by δ, on the right hand side (Bracewell, 1986).

$$\rho - x_1 \cos\varphi - x_2 \sin\varphi \xrightarrow{becomes} \delta(\rho - x_1 \cos\varphi - x_2 \sin\varphi)$$

The delta function δ, is the classical way to approach the line impulse, and has advantageous implications for dimensionality and integration of a line (Figure 10) (Bracewell, 1986). Such line integrals have a domain of infinity on the line and zero off the line (Bracewell, 1986).

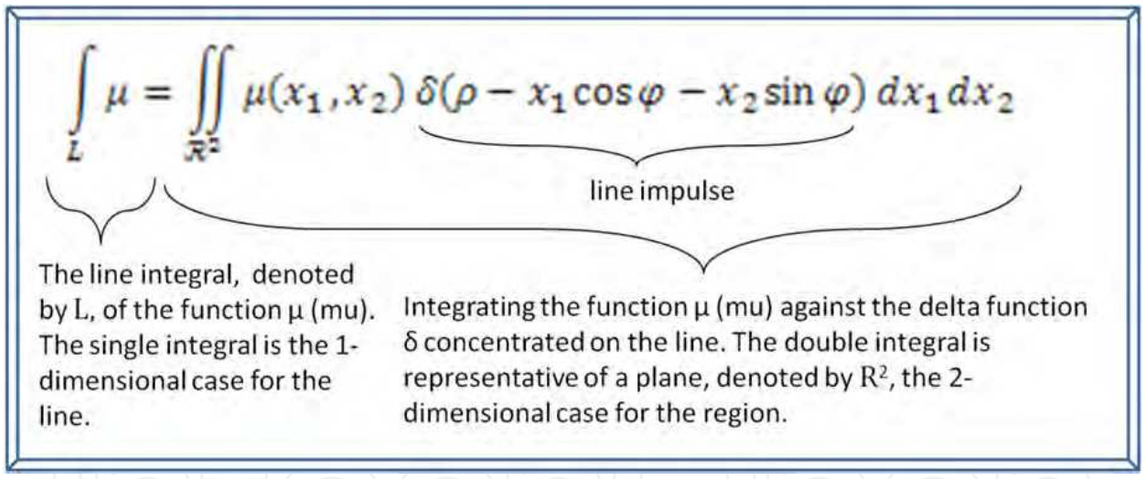

Fig. 10. Expansion of the line integral to an integral of a plane (2-dimensional space) containing the line impulse. The above notations of the integrals, L and R^2, are understood to have domains or "boundaries" from negative infinity (-∞) to infinity (∞).

The Radon transform

Equipped with a suitable coordinate system and having addressed the line integral with respect to the line impulse, we are ready to introduce the computational steps central to the mathematical model, inverting the Radon transform. As we do this, it is important to first point out what is varying as we work through the computations, i.e., to identify the variables associated with the integrand (those terms being integrated).

As shown below in Figure 11, superimposition of the useful/suitable coordinate system (as described earlier) onto a representative cross-sectional image (the region of interest) will help identify the variable.

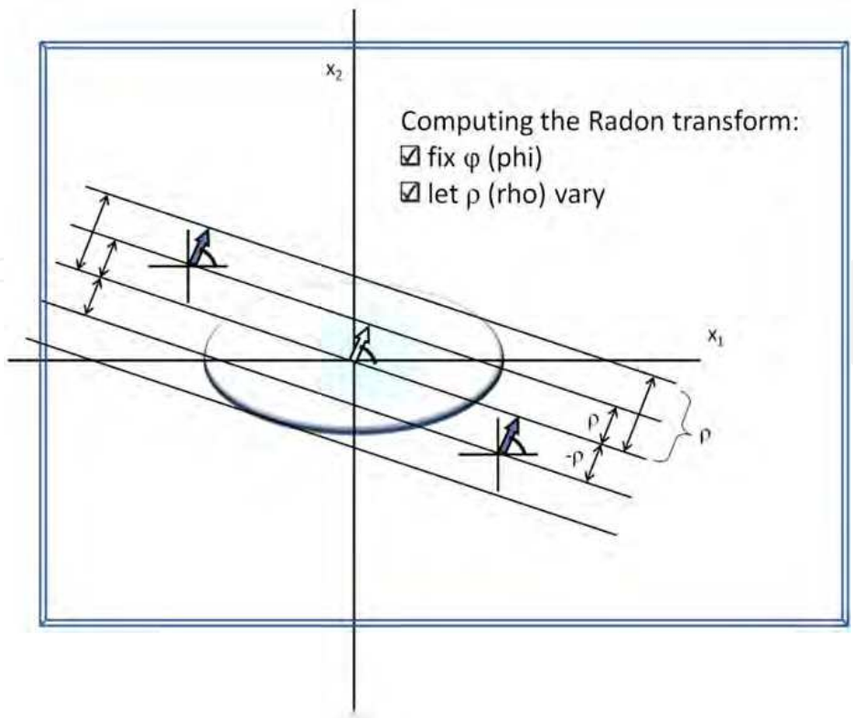

Fig. 11. Notice what this family of parallel lines has in common, each line has the same angle φ (phi) to the x_1-axis. Thus, the variable to use with respect to integrating the constituent integrals of the Radon transform (and those integrals contributing to the Fourier transform) is the distance ρ (rho) of a line from the line passing through the origin.

Looking at Figure 11, think in terms of what it means to fix φ (phi) and let ρ (rho) vary. This means the family of parallel lines will be defined by the angle made with the x_1-axis, and only the distance of a line from the line going through the origin will be of concern. In other words, the angle is fixed, it does not change, allowing ρ (rho) to be the variable as we accumulate (integrate) data. Thus, the Radon transform R can now be introduced by rewriting the equation from Figure 10 in greater detail (Bracewell, 1986), in relation to the signal/function μ (mu), where μ (mu) is a function of ρ (rho) and φ (phi), as shown below. ***Note: in this and the remaining sections, the x-ray signal will be written as the function μ (mu)***.

$$\mathcal{R}\mu(\rho,\varphi) = \int_{L(\rho,\varphi)} \mu = \int_{-\infty}^{\infty}\int_{-\infty}^{\infty} \mu(x_1, x_2)\, \delta\,(\rho - x_1\cos\varphi - x_2\sin\varphi)\, dx_1\, dx_2$$

Accordingly, both the line integral L and the double integral above are more concisely expressed here than that seen in Figure 10. With respect to the line integral, it is now written as a function of ρ (rho) and φ (phi), and the limits of integration (-∞ to ∞) are explicitly stated for the double integral.

As discussed earlier the Radon transform is a special case of the Fourier transform, thus it is accurate to write the Fourier transform F with respect to ρ (rho) (denoted by the subscript ρ) as a function of the Radon transform R, as seen in the following notation (Bracewell, 1986).

$$\mathcal{F}_{\rho}\big(\mathcal{R}\mu(\rho,\varphi)\big) = \int_{-\infty}^{\infty} e^{-2\pi i r\rho}\,\big(\mathcal{R}\mu(\rho,\varphi)\big)\,d\rho$$

The significance of this step is that we are now accounting for the spatial domain, denoted by the letter "r" in the complex exponential, $e^{-2\pi i r\rho}$ (Boyce & DiPrima, 2005). In reality, the derivation for this mathematical application (as we strive to understand it in the context of CT) is concerned with two domains, the spatial domain and the frequency domain, and moreover, both are present/available in the complex exponential, $e^{-2\pi i r\rho}$.

$$\mathcal{F}_{\rho}\big(\mathcal{R}\mu(\rho,\varphi)\big) = \int_{-\infty}^{\infty} e^{-2\pi i r\rho}\,\big(\mathcal{R}\mu(\rho,\varphi)\big)\,d\rho$$

$$= \int_{-\infty}^{\infty} e^{-2\pi i r\rho}\left(\int_{-\infty}^{\infty}\int_{-\infty}^{\infty} \mu(x_1,x_2)\,\delta\,(\rho - x_1\cos\varphi - x_2\sin\varphi)\,dx_1\,dx_2\right)d\rho$$

The right hand side of the Fourier transform $\mathcal{F}$ equality (top equation) contains the Radon transform $\mathcal{R}$ (underscored). It is subsequently rewritten (underscored) as the function μ (mu), as seen in Figure 3, to evaluate **the line impulse delta function δ (i.e., bursts of x-ray phenomena)**. Then, the selected (boxed) terms are switched to rearrange the order of integration and evaluate the single integral first (illustrated below).

$$= \int_{-\infty}^{\infty}\int_{-\infty}^{\infty} \mu(x_1,x_2)\left(\int_{-\infty}^{\infty} e^{-2\pi i r\rho}\,\delta\,(\rho - x_1\cos\varphi - x_2\sin\varphi)\,d\rho\right)dx_1\,dx_2$$

With the terms now rearranged and grouped together, the equation is set up to integrate the 1-dimensional Fourier transform (the single integral in parentheses), in order that we may later deal with the 2-dimensional Fourier transform (the double integral) to recover the densities contained in the function μ (mu), along the line/family of lines (i.e., the information concentrated in the trajectories of the x-rays in the exit beam). **Note: the delta function δ remains in place, ready to be integrated.**

Fig. 12. Illustrative drawing to explain the way in which the dimensionality of the model is handled as the mathematical derivation unfolds.

Refer to Figure 12 which shows the critical steps on how dimensionality is dealt with in the model. The 1-dimensional component is evaluated first, as described in Figure 12, and is rewritten below in bold type face for emphasis, note the left hand side of the equation below.

$$\int_{-\infty}^{\infty} \boldsymbol{e^{-2\pi i r\rho}\,\delta\,\big(\rho - (x_1\cos\varphi + x_2\sin\varphi)\big)d\rho} = e^{-2\pi i r(x_1\cos\varphi + x_2\sin\varphi)}$$

We see that the integral equates to the complex exponential, $e^{-2\pi i r(x_1\cos\varphi + x_2\sin\varphi)}$, which is rewritten after distributing the "r".

$$e^{-2\pi ir(x_1 \cos\varphi + x_2 \sin\varphi)} = e^{-2\pi i(x_1 r\cos\varphi + x_2 r\sin\varphi)}$$

To finish simplifying the complex exponential, we introduce the concept of dual variables, in that (x_1 is paired with ξ_1) and (x_2 is paired with ξ_2), where ξ_1 and ξ_2 are each constants defined in the following way:

$$\xi_1 = r\cos\varphi \quad \text{and} \quad \xi_2 = r\sin\varphi$$

Although it is noted that each of these equalities above suggest implementation of polar coordinates (the coordinate system employed for spherical/circular symmetry), they are not intended to do so in this derivation. The equalities merely serve as a means to express the complex exponential more simply with dual variables, as follows:

$$= e^{-2\pi i(x_1\xi_1 + x_2\xi_2)}$$

It is now important to emphasize what has been derived thus far, and what computational steps remain. The above result is the answer to the evaluation of the 1-dimensional integral described in Figure 12 (that integral involving the line impulse, which has now been computed). The remaining computational steps involve the actual processes to recover the values of the densities μ (mu), i.e., to reconstruct the densities from the region, by inverting the Radon transform as a function of the Fourier transform over 2-dimensional region.

Inverting the Radon transform

To invert the Radon transform, we first plug the result of the 1-dimensional integral (as derived above and in bold type face below) back into the original Fourier transform which we set up earlier. This is shown below. We now have the 2-dimensional Fourier transform of μ (mu), i.e., the double integral, set up to integrate first with respect to dx_1 and then with respect to dx_2.

$$\mathcal{F}_\rho\big(\mathcal{R}\mu(\rho,\varphi)\big) = \int_{-\infty}^{\infty}\int_{-\infty}^{\infty} \mu(x_1, x_2)\, \boldsymbol{e^{-2\pi i(x_1\xi_1 + x_2\xi_2)}}\, dx_1\, dx_2$$

Hence, to best convey the details of the final computation step, it is of certain benefit to pause in order to recapitulate the entire mathematical derivation up to this point.

1. A suitable coordinate system (ρ,φ) was found.
2. φ (phi) was fixed to let ρ (rho) vary, where φ (phi) is the angle that each line in the family of parallel lines makes with the x_1-axis, and ρ (rho) represents the values of distances of these lines from the line passing through the origin.
3. The 1-dimensional Fourier transform of the corresponding Radon transform was found with respect to ρ (rho), resulting in the 2-dimensional Fourier transform of μ (mu).
    a. In principle the problem is solved. We have measured the Radon transform, i.e., the line integral of μ (mu) along the family of parallel lines.
    b. Because we know the 1-dimensional transform expression and the values which emerge, those associated with $[\, e^{-2\pi i(x_1\xi_1 + x_2\xi_2)}]$, we can now compute the Fourier transform with respect to ρ (rho) (Bracewell, 1986).

By computing the Fourier transform with respect to ρ (rho), we get the 2-dimensional Fourier transform with respect to μ (mu). This means that we can find μ (mu) by taking the inverse of the 2-dimensional Fourier transform of what was found:

$$\mathcal{F}\mu(\xi_1,\xi_2) = \mathbb{G}(\xi_1,\xi_2) \xrightarrow{recovers\ \mu} \mu = \mathcal{F}^{-1}\mathbb{G}(\xi_1,\xi_2)$$

where $\mathbb{G}(\xi_1,\xi_2)$ equals ($e^{-2\pi i(x_1\xi_1+x_2\xi_2)}$), the known values of the 1-dimensional Fourier transform. By taking the inverse of the signal/function μ (mu) (we recover the lost data contained in the trajectory lines of the x-ray photons passing through the region of interest), and we are able to reconstruct the densities of the region (Bracewell, 1986). That is to say, we now have μ (mu). *In turn, this enables the CT scanner to assign density values according to the Hounsfield unit scale of CT numbers for data acquisition/image processing* (Jackson & Thomas, 2004).

In summary, the goal of this section was to familiarize interventional pain physicians with the equations that ultimately underscore quality control algorithms for CT scanners and provide a footprint to build quality assurance protocols for CT scanning to help reduce risks of radiation overexposure. Accordingly, the derivation presented here represents the mathematical framework employing the parallel beam model. Ideally, to make the model practical, and to implement it numerically, discrete versions need to be rooted in the steps above, and certain computation issues, such as the playoff between Cartesian and polar coordinate representations, need to be dealt with.

Acknowledgements: The author thanks Stanford University Engineering for open access to EE261 The Fourier Transform and Its Applications as taught by Brad Osgood, PhD, as well as acknowledges John Labowsky for his technical critique of this section.

3.3 Triplanar imaging in pain medicine procedures: Conventional-CT guidance and CT-fluoroscopy

In the 1990s conventional-CT guidance began to be used by interventionally-trained pain physicians for chronic benign spinal pain (Aguirre et al., 2005; Gangi et al., 1998). During this period, algorithms were also developed to establish CT-fluoroscopy, which introduced a real-time feature to this modality (Daly & Templeton, 1999). Accordingly, CT-fluoroscopy has become a powerful imaging tool (Meleka, 2005). To this point, interventional pain techniques have been proposed and studied under this imaging technique, such as treatment of coccydynia by targeting the ganglion impar (Datir et al., 2010) or the efficacy of lumbar sympathetic blocks (Schmid, 2006). Interestingly, the literature remains sparse for pain procedure-specific dosimetry reports relative to CT, although Table 8 highlights the work in this area by Wagner (2004a, 2004b). In this light, the interested reader performing CT-guided pain procedures (or interested in being trained for such procedures) may wish to initiate dosimetry studies, since all radiologic based procedures should be evaluated specifically and the knowledge gained disseminated to help follow ALARA principles for patients and personnel radiation exposure (and hence, optimize health physics strategies).

3.4 Radiation risk management/safety

While CT-fluoroscopy may decrease patient absorbed dose by 94% compared to conventional CT (Meleka et al., 2005), others argue that the radiation exposure may not be justified, especially when other modalities can be used which eliminate the need for such exposure altogether, such as CT-guided (Thoumas et al., 1999) versus ultrasound-guided (Gruber & Bodner, 2004) pudendal nerve blocks. In cases were CT guidance has shown to be clearly beneficial, the lower doses associated with CT-fluoroscopy have been attributed to

intermittent exposure techniques and/or exposure parameters, such as lower tube current (Meleka et al., 2005). Moreover, strategies have also emerged to help reduce occupational radiation dose. For example, the use of lead shields, or as previously discussed, the use of lead aprons. In addition, the use of needle holders, when feasible during the procedure, avoids physician hand placement directly into the x-ray beam (Kato, 1996).

Kato **1996**	Wagner **2004a**	Wagner **2004b**	CT-Fluoroscopy
			• Lumbar Selective Nerve Root Block
–	2	–	CT-Fluoroscopy Time
–	7.3	–	o Patient Effective Dose
–	390	–	o Effective Dose (Total) Physician
			• Lumbar Epidural
		Not specified	CT-Fluoroscopy Time
–	–	> 1	o Effective Dose (Physician/Procedure)
–	–	75	o Effective Dose (Total) Physician
			• Effective Dose (given in microSieverts per second)
1140	–	–	o Physician Hand

Key: CT-Fluoroscopy time (in seconds); effective dose (in microSieverts).

Table 8. CT-Fluoroscopy exposure metrics.

4. Ultrasound and interventional pain medicine

4.1 The ultrasound imaging chain

Continued research in the area of medical imaging has led to the development of compact and durable ultrasound scanners with improved imaging capabilities. Nevertheless, the basic instrumentation and underlying principles of this modality remain the same. The ultrasound imaging chain is considered a "closed" loop made up of the following links: a transmitter, a transducer, a receiver, and the image viewing system (Aldrich, 2007). Note that the physical phenomenon behind image creation is the piezoelectric effect, or stated more explicitly it is the effect on and induced by deformations of piezoelectric crystals embedded within materials housed inside the transducer which enables mechanical energy to be transformed into ultrasonic impulses—and vice versa for signal processing.

Upon interaction with tissue, ultrasonic waveforms may be 1) transmitted through the tissue, 2) undergo reflection (echo) or refraction (bending) at tissue boundaries, or 3) the acoustic energy may be attenuated. Surfaces that **reflect** these sound waves are classified as either *specular reflectors* or *scattering reflectors*. An example of the former is the needle, whereas an example of the latter is the interface between neural and adjacent tissues. Thus, it is the reflected sound waves (i.e., the available energy contained in the echoes collected at the transducer) which contribute to a meaningful image. **Refracted** sound waves are those which change direction due to slight differences at the boundary (i.e., edge) between two tissue types. We note that such waves may not contribute to successful imaging if a significant amount of the propagated waveform is lost. Finally, with similarities which evoke comparisons to the attenuated x-ray beam, the attenuation of sound beams conveys a loss of energy as the ultrasonic waveforms are absorbed by the tissue. According to Sites et al. (2007):

> While attenuation can have a profound negative impact on image quality, there are two important adjustments that can be made on the ultrasound machine that help to overcome

some of the effects of attenuation. First, most machines allow the operator to artificially increase (or decrease) the signal intensity of the return echoes from all points in the displayed field. This is accomplished by adjusting the gain control higher to increase the overall brightness. Second, most machines offer the operator the ability to control gain independently at specified depth intervals. This is known as time gain compensation. The time gain compensation should be progressively increased as the depth of penetration increases in order to compensate for the corresponding loss of signal intensity.

It is also interesting to note that *attenuation is inversely related to waveform frequency*, and that this relationship is nontrivial with respect to image resolution (i.e., recorded detail or the ability to distinguish between objects) and ultrasound physics. In the following subsection, which highlights the physics behind ultrasound imaging, we will further explore this relation to better understand the clinical impact of sound wave attenuation.

4.2 Waveform propagation in tissue: The physics of ultrasound

Based on waveform physics, that is, frequency, amplitude, and wavelength, the principles of ultrasound are unified by the foregoing description. A pulse of sound is emitted from a source (i.e., the transducer) and travels outward through a medium. If an object reflects the wave, then acoustic energy travels back to the source and is detected as an echo at the source. Thus, at a known speed (the speed of sound of the surrounding medium), the waveform travels a distance equal to twice the distance from the source to the reflected object (Kane, 2009). The basic equation follows:

$$L = (V_S \cdot T)/2$$

where L is twice the distance from the source to the object, V_S is the speed of sound of the surrounding medium, and T is time. Note: the average value of V_S in soft tissue is 1540 m/s. The ultrasound scanner records the time required for each pulse to return, and then uses the speed of sound to calculate the distance of the object. See Figure 13. Echo intensity is indicated by plotting a variety of intensities on the monitor subsequent to a gray-scale (white to gray to black). Thus, brightness is a consequence of a mapping of echo intensity versus position; hence this viewing algorithm/mode is named B-scan, where "B" means brightness.

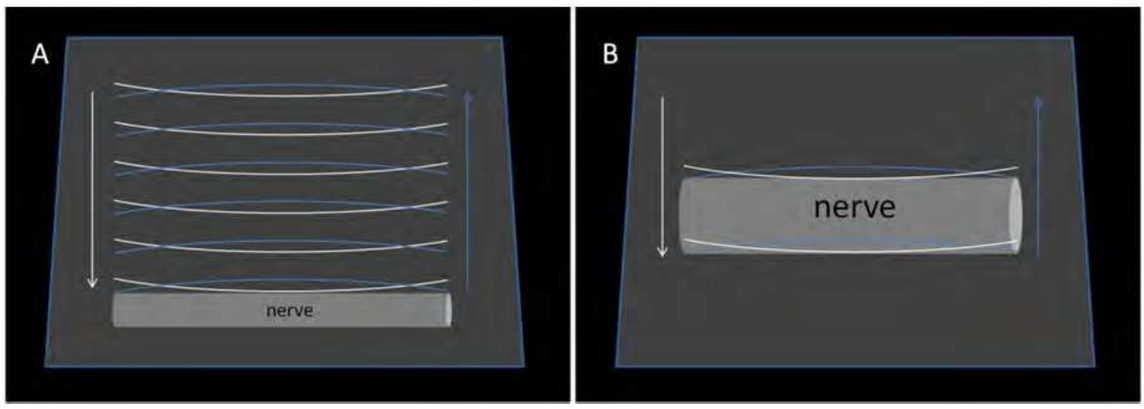

Fig. 13. Panel-A shows a target nerve (or scattering reflector) and direction of travel of incident sound waves (white) and echoes (blue). Panel-B shows a zoomed-in view of the same nerve to more closely exhibit the reflection of sound waves from near and far tissue borders (with respect to the transducer).

As emphasized in the above subsection, a nontrivial inverse relationship exists between attenuation and waveform frequency. We will now look more closely at this relation.
The most important aspects of ultrasound image resolution are those which govern axial, lateral, and temporal resolution—*in which all three together comprise spatial resolution*. **Axial resolution** is the ability to distinguish two structures at different depths, parallel to the direction of the ultrasound beam. Furthermore, it is approximately equal to one half of the ultrasound pulse length. In other words, if the distance between two objects is greater than one half of the pulse length, then the objects will appear as two distinct structures. It follows that higher waveform frequencies (short pulse lengths) produce the best axial resolution. However, because of the existing inverse relationship, higher frequency waveforms are more readily attenuated, and thus, tissue penetration is sacrificed. **Lateral resolution** is the ability to distinguish two structures at the same depth, perpendicular to the direction of the ultrasound beam. High frequency and focused ultrasound beams produce the narrowest beams, thus maximizing lateral resolution, but once again tissue penetration is sacrificed. Finally, **temporal resolution** relates to frame rate, and therefore, the ability to distinguish between real-time imaging and motion artifacts. During nerve blocks in regional anesthesia for example, motion artifacts occur with movement of the probe/transducer, or during needle insertion, or with injection of the anesthetic agent. Ultimately, temporal resolution is limited by the sweep speed (activation of the piezoelectric crystals) of the ultrasound beam, which in turn is limited by the speed of sound in tissue. Attempts to control temporal resolution consist of 1) increasing the sweep speed or 2) decreasing the scanning angle (applicable to phased array probes only). The first option decreases the lateral resolution, and the second option decreases the field of view. Thus, not only do we see an interconnected relationship with respect to image resolution, but at present, adjustments available to try to improve resolution are restrained by the laws of waveform physics. That is to say, despite the progress made in ultrasound equipment and technology (which we will highlight in the accompanying discussion on regional anesthesia), ultrasound imaging is, in reality, a tradeoff between spatial resolution and achievable depth of imaging (Sites et al., 2007).

4.3 Ultrasound guidance in pain medicine: Regional anesthesia

The use of ultrasound for image guidance in regional anesthesia has several practical benefits (Sites et al., 2009), the foremost being that ionizing radiation is not necessary for image production enabling ultrasound machines to be highly portable. Case series and small-scaled outcomes studies with respect to nerve blocks have purported shortened procedure times and faster block onset; increased patient satisfaction; and fewer block-related complications (Marhofer & Chan, 2007). As far as limitations, there are two primary considerations: 1) resolution and image quality vary inversely with depth of penetration, as previously discussed; and 2) needle tracking for in-plane needle entry is a challenge in part because the needle is not visible on the monitor (Marhofer & Chan, 2007). However, with respect to in-plane needle tracking, one company (SonoSite, Inc.) has developed an ultrasound system to remedy this problem. By sending out a "secondary beam" at a 45° angle from the transducer for perpendicular beam-to-needle alignment established outside the region of interest, needle visualization is optimized. This enables the physician to see the needle's approach to the target nerve within the field of view. In addition, to help improve therapeutic accuracy of ultrasound-guided pain medicine, the ultrasound characteristics of needles have been described (Maecken et al., 2007), "echo-friendly" needle designs have been developed (Deam, 2007), and the benefits of three-dimensional (3D) ultrasound

imaging has been investigated (Feinglass et al., 2007; Foxall, et al., 2007). Moreover, cutting edge ultrasonic technological advances have introduced image-enhanced tissue staining to remotely palpate the target nerve of interest using acoustic radiation force imaging to both improve accuracy and limit variability in regional anesthesia (Palmeri et al., 2008; Nightingale et al., 2001).

4.4 Risk management: Ultrasound safety

While there are no known absolute contraindications in ultrasound imaging, the position of The U.S. Food and Drug Administration (FDA) (n.d.) concerning ultrasound safety follows.

> Ultrasound imaging has been used for over 20 years and has an excellent safety record. It is non-ionizing radiation, so it does not have the same risks as x-rays or other types of ionizing radiation. Even though there are no known risks of ultrasound imaging, it can produce effects on the body. When ultrasound enters the body, it heats the tissues slightly. In some cases, it can also produce small pockets of gas in body fluids or tissues (cavitation). The long-term effects of tissue heating and cavitation are not known.

For a more in-depth discussion on tissue sensitivity relative to interpreting risk from exposure to ultrasound imaging, the reader is encouraged to study the report on this topic issued by members of the World Federation for Ultrasound in Medicine and Biology Safety Committee (Barnett et al., 1997).

5. Future directions in interventional pain medicine

5.1 *The promise of real-time three-dimensional (3D) fluoroscopy

While CT-fluoroscopy offers unique viewing perspectives with overall imaging capabilities (as discussed in the earlier section, "Triplanar Imaging in Pain Medicine Procedures: Conventional-CT Guidance and CT-Fluoroscopy"), interestingly, real-time 3D imaging has not been reported. Conversely, although real-time 3D ultrasound has been show to be beneficial in regional anesthesia (as cited in the above section, "Ultrasound guidance in Pain Medicine: Regional Anesthesia"), ultrasound imaging does not offer the allure that fluoroscopy enjoys with respect to image resolution, particularly of bony anatomy.

Technology is currently available to fit mobile C-arm fluoroscopy systems with 3D imaging capabilities (Stübig et al., 2009; Izadpanah et al., 2009; Villavicencio et al., 2005). (Note: current fluoroscopy systems creating 3D imagery are limited to 150°—360° with mechanical orientation or manipulation or post-processing.) Notably, the limiting factor in the utility of these systems under most interventional pain protocols is image construction time. However, one company, Imaging3 Inc., claims to have developed signal processing algorithms to produce 3D high-resolution fluoroscopic images in *real-time* via its "Dominion" platform. (Note: at the time of this publication, this device has *not* received FDA clearance.) The design is built around a dedicated O-arm—a gantry similar to that used in CT—to allow continuous 360° rotation of the x-ray tube and scintillation detector with on-demand imaging of the patient under continuous or pulsed fluoroscopy. (See the earlier discussion on radiation risk management in fluoroscopy to review the advantages of pulsed fluoroscopy.) This approach is expected to allow imaging of the patient from any frame of reference or angulation. Intended use is anticipated by the company to be procedures in which multiple frames of reference are required. From a pain medicine perspective, real-time 3D fluoroscopic guidance may be possible for discography, vertebral augmentation, percutaneous lumbar decompression, facet rhizotomy, or intradiscal electrothermal therapy.

In addition, it is projected that the Dominion will offer a multi-modal feature to give physicians the ability to view cross-sectional anatomy by emulating CT, using a cone-beam CT model.

*Note: neither the author nor anyone known to the author has any relationship with any of the companies mentioned in this subsection. This includes but is not limited to financial, consulting, and business relationships. All information was obtained through company filings and/or press releases and/or marketing literature.

5.2 *Interventional magnetic resonance imaging (MRI)

This section presents a brief discussion on the concept of MRI-guided procedures. Whereas the use of MRI for this purpose is in its infancy, the intent of MRI-guided/interventional scanning is to assist physicians during intra-operative, and diagnostic and therapeutic procedures using magnetic-compatible instrumentation. The Fonar 360™ MRI unit represents the cutting edge in technology for this vision. The Fonar 360™ is a specialized MRI design with the field and gradient magnets encapsulated in the ceiling and floor of a dedicated, monolithic room. In this capacity, the enlarged room-sized magnet and the 360° access to the patient permits full-fledged medical teams to walk into the room (i.e., "inside the magnet") to interact with the patient. The first unit was installed at the Nuffield Orthopaedic Centre in Oxford, United Kingdom.

Another developer, MRI Interventions Inc., a medical device maker focusing on interventional MRI applications, has obtained FDA clearance on their ClearPoint® system which is designed to enable minimally invasive procedures in the brain—namely to facilitate image guidance for the introduction of deep brain stimulation leads—utilizing a hospital's existing MRI suite. On this note, although to date the use of deep brain stimulation for pain is limited due to lackluster outcomes (Levy et al., 1987; Coffey, 2001; Hamani et al., 2006), research is ongoing to find appropriate surgical candidates and areas in the brain conducive to long-term efficacy for conditions with a central pain aspect. Such targeted brain centers currently under investigation are the ventral capsule/ventral striatum in thalamic pain syndrome (U.S. National Institutes of Health [NIH], NCT 01072656). On another note, the introduction of deep brain stimulation systems with "steerable" field currents (the VANTAGE trial) (NIH, NCT 01221948) may ultimately prove clinically advantageous in such approaches to pain management.

Finally, our discussion on interventional MRI would be incomplete without reference made to patient care and concerns about biologic effects relative to exposure to MRI. Hence, we refer the reader to the collection of work by Frank Shellock. On this point, we encourage the reader to begin with Shellock and Cruse (2004) to gain an overview on tissue sensitivity associated with gradient magnetic fields, acoustic noise, and radiofrequency fields/radiation in MRI.

*Note: neither the author nor anyone known to the author has any relationship with any of the companies mentioned in this subsection. This includes but is not limited to financial, consulting, and business relationships. All information was obtained through company filings and/or press releases and/or marketing literature.

5.3 Ultrasound imaging: Beyond regional anesthesia

With ultrasound guidance for nerve blocks in regional anesthesia established, intriguing applications of this modality in pain medicine are beginning to surface. For example, ultrasound guidance for trigger point injection therapy has been shown to be comparable to

electromyographic guidance (Botwin et al., 2008). One advantage of this technique is that in the cervicothoracic area, the physician can see the lungs in order to guard against inadvertent procedure-induced pneumothorax. In other applications, the use of ultrasound was also recently documented as the modality of choice to facilitate placement of percutaneous leads in two peripheral nerve stimulation trialing procedures to treat ilioinguinal neuralgia (Carayannopoulos et al., 2009). This marked a new era in ultrasound-guided pain medicine, as well as technical improvement and refinement of a surgical technique. Likewise, image guidance with ultrasound in pain procedures traditionally reserved for x-ray producing modalities (fluoroscopy) have been reported. The evidence for this is gleaned from reports on real-time ultrasound-guided epidural injections (Karmakar, 2009), and even the introduction of current procedural terminology codes for transforaminal epidural injections and paravertebral/facet injections.

However, more compelling evidence for the versatility of ultrasound in pain medicine is found in its utility in pain-related physical rehabilitation (a role for this modality which is in its infancy) (Peolsson & Brodin, 2009; Primack, 2010; Wininger, 2010). It is well recognized that when musculoskeletal injuries/syndromes induce pain, use of the involved body part (such as the shoulder for example) becomes limited, which may in turn cause more pain and more limited use and a vicious cycle is started, possibly leading to physical limitation that negatively influences the quality of life of the patient. Alternatively, qualitative and quantitative description of musculoskeletal tissue dynamics and coordination during real-time procedures is possible through ultrasound imaging via tissue velocity imaging. This technique may be used to scrutinize both intra-muscular and inter-muscular coordination patterns (Peolsson & Brodin, 2009). Dynamic imaging using ultrasound to assess shoulder impingement syndromes is another example of pain-related physical rehabilitation ultrasound use (Bureau et al., 2006). To this point, it is noteworthy to mention that researchers have looked into how the overall utility of musculoskeletal ultrasound imaging impacts MRI. It was discovered that selective substitution of musculoskeletal ultrasound for MRI can result in significant cost savings to the health care system, but issues related to accuracy, variability, education and competence need to be further addressed (Jacobson, 2009).

6. References

AAPM. Cardiac catheterization equipment performance. (2001). American Association of Physicists in Medicine. Report Series No. 70.

Aguirre DA, Bermudez S, & Diaz OM. (2005). Spinal CT-guided interventional procedures for management of chronic back pain. *J Vasc Interv Radiol*, vol. 16, no. 5, pp. 689-697.

Aldrich JE. (2007). Basic physics of ultrasound imaging. *Crit Care Med*, vol. 35, no. 5, pp. S131-S137.

Aufrichtig R, Xue P, Thomas CW, Gilmore GC, & Wilson DL. (1994). Perceptual comparison of pulsed and continuous fluoroscopy. *Med Phys*, vol. 21, no. 2, pp. 245-256.

Back DL, Hilton AI, Briggs TW, Scott J, Burns M, & Warren P. (2005). Radiation protection for your hands. *Injury*, vol. 36, no. 12, pp. 1416-1420.

Barnes JE. (1992). Characteristics and control of contrast in CT. *Radiographics*, vol. 12, no. 4, pp. 825-837.

Barnett SB, Rott HD, ter Haar GR. Ziskin MC, Maeda K. (1997). The sensitivity of biological tissue to ultrasound. *Ultrasound Med Biol*, vol. 23, no. 6, pp. 805-812.

Balter S. (2006). Methods for measuring fluoroscopic skin dose. *Pediatr Radiol*, vol. 36, suppl. 2, pp. 136-140.

Balter S. (2008). Capturing patient doses from fluoroscopically based diagnostic and interventional systems. *Health Phys*, vol. 95, no. 5, pp. 535-540.

Boszczyk BM, Bierschneider M, Panzer S, et al. (2006). Fluoroscopic radiation exposure of the kyphoplasty patient. *Eur Spine J*, vol. 15, no. 3, pp. 347-355.

Botwin KP, Freeman ED, Gruber RD, et al. (2001). Radiation exposure to a physician performing fluoroscopically guided caudal epidural steroid injections. *Pain Physician*, vol. 4, no. 4, pp. 343-348.

Botwin KP, Thomas S, Gruber RD, et al. (2002). Radiation exposure of the spinal interventionalist performing fluoroscopically guided transforaminal epidural steroid injections. *Arch Phys Med Rehabil*, vol. 83, no. 5, pp. 697-701.

Botwin KP, Fuoco GS, Torres FM, et al. (2003). Radiation exposure to the spinal interventionalist performing lumbar discography. *Pain Physician*, vol. 6, no. 3, pp. 295-300.

Botwin KP, Sharma K, Saliba R, & Patel BC. (2008). Ultrasound-guided trigger point injections in the cervicothoracic musculature: a new and unreported technique. *Pain Physician*, vol. 11, no. 6, pp. 885-889.

Boyce WE, DiPrima RC. (2005). *Elementary Differential Equations*. 8th ed. John Wiley & Sons, Inc; Hoboken, NJ.

Bracewell RN. (1986). *The Fourier Transform and Its Applications*. 3rd ed. McGraw Hill. Singapore.

Bureau NJ, Beauchamp M, Cardinal E, & Brassard P. (2006). Dynamic sonography evaluation of shoulder impingement syndrome. *AJR Am J Roentgenol*, vo. 187, no. 1, pp. 216-220.

Bushong SC. (2004). Radiation protection procedures. In: Bushong SC, ed. *Radiologic Science for Technologists: Physics, Biology, and Protection*. 8th ed. pp. 583-601, Mosby Inc., St. Louis, Mo.

Carayannopoulos A, Beasley R, & Sites B. (2009). Facilitation of percutaneous trial lead placement with ultrasound guidance for peripheral nerve stimulation trial of ilioinguinal neuralgia: a technical note. *Neuromodulation*, vol. 12, no. 4, pp. 296-301.

Carlton RR, Adler AM. (2006). *Principles of Radiographic Imaging: An Art and a Science*. 4th ed. Clifton Park, NY: Thomson Delmar.

Clasper JC, Pinks T. (1995). Technical note: an assessment of x-ray protective gloves. *Br J Radiol*, vol. 68, no. 812, pp. 917-919.

Christodoulou EG, Goodsitt MM, Larson SC, Darner KL, Satti J, & Chan HP. (2003). Evaluation of the transmitted exposure through lead equivalent aprons in a radiology department, including the contribution from backscatter. *Med Phys*, vol. 30, no. 6, pp. 1033-1038.

Coffey RJ. (2001). Deep brain stimulation for chronic pain: results of two multicenter trials and a structured review. *Pain Med*, vol. 2, no. 3, pp. 183-192.

Cousin AJ, Lawdahl RB, Chakraborty DP, & Koehler RE. (1987). The case for radioprotective eyewear/facewear. Practical implications and suggestions. *Invest Radiol*, vol. 22, no. 8, pp. 688-692.

Daly B, Templeton PA. (1999). Real-time CT fluoroscopy: evolution of an interventional tool. *Radiology*, vol. 211, no. 2, pp. 309-315.

Datir A, Connell D. (2010). CT-guided injection for ganglion impar blockade: a radiological approach to the management of coccydynia. *Clin Radiol*, vol. 65, no. 1, pp. 21-25.

Davies AG, Cowen AR, Kengyelics SM, et al. (2006). X-ray dose reduction in fluoroscopically guided electrophysiology procedures. *PACE*, vol. 29, no. 3, pp. 262-271.

Deam RK, Kluger R, Barrington MJ, & McCutcheon CA. (2007). Investigation of a new echogenic needle for use with ultrasound peripheral nerve blocks. *Anaesth Intensive Care*, vol. 35, no. 4, pp. 582-586.

Deshpande KK, Wininger KL. (2011). Feasibility of combined epicranial temporal and occipital neurostimulation: treatment of a challenging case of headache. *Pain Physician*, vol. 14, no. 1, pp. 37-44.

Dowd SB, Tilson ER. (1999). *Practical Radiation Protection and Applied Radiobiology*. 2nd ed. Philadelphia, Pa: Saunders.

Fazel R, Krumholz HM, Wang Y, et al. (2009). Exposure to low-dose ionizing radiation from medical imaging procedures. *N Eng J Med*, vol. 361, no. 9, pp. 849-857.

Feinglass NG, Clendenen SR, Torp KD, Wang RD, Castello R, & Greengrass RA. (2007). Real-time three-dimensional ultrasound for continuous popliteal blockade: a case report and image description. *Anesth Analg*, vol. 105, no. 1, pp. 272-274.

Ferreira CC, Galvão LA, Veira JW, Maia AF. (2010). Validation of an exposure computational model to computed tomography. *Brazilian Journal of Physics Médica*, vol. 4, no. 1, pp. 19-22.

Finnerty M, Brennan PC. (2005). Protective aprons in imaging departments: manufacturer stated lead equivalence values require validation. *Eur Radiol*, vol. 15, no. 7, pp. 1477-1484.

Fish DE, Kim A, Ornelas C, Song S, & Pangarkar S. The risks of radiation exposure to the eyes of the interventional pain physician. *Radiology Research and Practice*, vol. 2011. Article ID 609537, 5 pages, 2011. doi:10.1155/2011/609537.

Foxall GL, Hardman JG, Bedforth NM. (2007). Three-dimensional, multiplanar, ultrasound-guided, radial nerve block. *Reg Anesth Pain Med*, vol. 32, no. 6, pp. 516-521.

Gangi A, Dietemann JL, Mortazavi R, Pfleger D, Kauff C, & Roy C. (1998). CT-guided Interventional procedures for pain management in the lumbosacral spine. *Radiographics*, vol. 18, no. 3, pp. 621-633.

Geleijns J, Wondergem J. (2005). X-ray imaging and the skin: Radiation biology, patient dosimetry and observed effects. *Rad Prot Dos*, vol. 114, no. 1-3, pp. 121-125.

Kapural L, Goyle A. (2007). Imaging for provocative discography and minimally invasive percutaneous procedures for treatment of discogenic lower back pain. *Tech Reg Anesth Pain Manag*, vol. 11, no. 2, pp. 73-80.

Gruber H, Bodner G. (2004). Why CT guided? [comment]. *AJR Am J Roentgenol*, vol. 182, no. 3, p. 824.

Hamani C, Schwalb JM, Rezai AR, Dostrovsky JO, Davis KD, Lozano AM. (2006). Deep brain stimulation for chronic neuropathic pain: long-term outcome and the incidence of insertional effect. *Pain*, vol. 125, no. 1, pp. 188-196.

Izadpanah K, Konrad G, Südkamp NP, & Oberst M. (2009). Computer navigation in balloon kyphoplasty reduces the intraoperative radiation exposure. *Spine*, vol. 34, no. 12, pp. 1325-1329.

Jackson S, Thomas R. (2004). Introduction to CT physics. *Cross-Sectional Imaging Made Easy*. p. 7, Churchill Livingston; Edinburgh, Scotland. 2004.

Jacobson JA. (2009). Musculoskeletal ultrasound: focused impact on MRI. *AJR Am J Roentgenol*, vol. 193, no. 3, pp. 619-627.

Johns HE, Cunningham JR. (1983). The interaction of ionizing radiation with matter. In: *The Physics of Radiology*. 4th ed. pp. 133-164, Thomas, Springfield, IL.

Johnston J, Killion JB, Vealé B, & Comello R. (2011). U.S. technologists' radiation exposure perceptions and practices. *Radiol Technol*, vol. 82, no. 4, pp. 311-320.

Kallmes DF, O E, Roy SS, et al. (2003). Radiation dose to the operator during vertebroplasty: prospective comparison of the use of 1-cc syringes versus an injection device. *AJNR Am J Neuroradiol*, vol. 24, no. 6, pp. 1257-1260.

Kane SA. (2009). *Introduction to Physics in Modern Medicine*. 2nd ed. Boca Raton, Fl: CRC Press.

Karmaka MK, Li X, Ho AM, Kwok WH, & Chui PT. (2009). Real-time ultrasound-guided paramedian epidural access: evaluation of a novel in-plane technique. *Br J Anaesth*, vol. 102, no. 6, pp. 845-854.

Kato R, Katada K, Anno H, Suzuki S, Ida Y, Koga S. (1996). Radiation dosimetry at CT fluoroscopy: physician's hand dose and development of needle holders. *Radiology*, vol. 201, no. 2, pp. 576-578.

Kosek P, Morgan D, Dunn J, et al. Electronically generated lead (EGL) scan: report of first clinical use. [abstract]. *North American Neuromodulation Society*. Dec. 7-9, 2006.

Levy RM, Lamb S, & Adams JE. (1987). Treatment of chronic pain by deep brain stimulation: long term follow-up and review of the literature. *Neurosurgery*, vol. 21, no. 6, pp. 885-893.

Larson R, Hostetler B, & Edwards BH. (2007). Calculus: Early Transcendental Functions. 4th ed. Houghton Mifflin Company; Boston, MA.

Little MP, Wakeford R, Tawn EJ, Bouffler SD, & Berrington de Gonzalez A. (2009). Risks associated with low doses and low dose rates of ionizing radiation: why linearity may be (almost) the best we can do. *Radiology*, vol. 251, no. 1, pp. 6-12.

Maecken T, Zenz M, & Grau T. (2007). Ultrasound characteristics of needles for regional anesthesia. *Reg Anesth Pain Med*, vol. 32, no. 5, pp. 440-447.

Mahesh M. (2001). Fluoroscopy: patient radiation exposure issues. *Radiographics*, vol. 21, no. 4, pp. 1033-1045.

Manchikanti L, Cash KA, Moss TL, & Pampati V. (2002). Radiation exposure to the physician in interventional pain management. *Pain Physician*, vol. 5, no. 4, pp. 385-393.

Manchikanti L, Cash KA, Moss TL, & Pampati V. (2003a). Effectiveness of protective measures in reducing risk of radiation exposure in interventional pain management: a prospective study. *Pain Physician*, vol. 6, no. 3, pp. 301-305.

Manchikanti L, Cash KA, Moss TL, Rivera J, & Pampati V. (2003b). Risk of whole body radiation exposure and protection measures in fluoroscopically guided interventional techniques: a prospective evaluation. *BMC Anesthesiol*, vol. 3, no. 1, p. 2.

Manchikanti L, Singh V, Pampati V, Smith HS, & Hirsch J. (2009). Analysis of growth of interventional techniques in managing chronic pain in the Medicare population: A 10-year evaluation from 1997 to 2006. *Pain Physician*, vol. 12, no. 1, pp. 9-34.

Marhofer P, Chan VWS. (2007). Ultrasound-guided regional anesthesia: current concepts and future trends. *Anesth Analg*, vol. 104, no. 5, pp. 1265-1269.

McKetty MH. (1998). The AAPM/RSNA physics tutorial for residents. X-ray attenuation. *Radiographics*, vol. 18, no. 1, pp. 151-163.

Meleka S, Patra A, Minkoff E, & Murphy K. (2005). Value of CT fluoroscopy for lumbar facet blocks. *AJNR Am J Neuroradiol*, vol. 26, no. 5, pp. 1001-1003.

Nightingale KR, Palmeri ML, Nightingale RW, & Trahey GE. (2001). On the feasibility of remote palpation using acoustic radiation force. *J Acoust Soc Am*, vol. 110, no. 1, pp. 625-634.

Oritz AO, Natarajan V, Gregorius DR, & Pollack S. (2006). Significantly reduced radiation exposure to operators during kyphoplasty and vertebroplasty procedures: methods and techniques. *AJNR Am J Neuroradiol*, vol. 27, no. 5, pp. 989-994.

Palmeri ML, Dahl JJ, MacLeod D, Grant S, & Nightingale KR. Regional anesthesia guidance using acoustic radiation force imaging. [abstract]. Proceedings of the Seventh International Conference on the Ultrasonic Measurement and Imaging of Tissue Elasticity. Oct. 27-30, 2008.

Peolsson M, Brodin LA. (2009). Functional musculoskeletal ultrasound. *European Musculoskeletal Review*, vol. 4, no. 2, pp. 102-107.

Perisinakis K, Damilakis J, Theocharopoulos N, Papadokostakis G, Hadjipavlou A, & Gourtsoylannis N. (2004). Patient exposure and associated radiation risks from fluoroscopically-guided vertebroplasty or kyphoplasty. *Radiology*, vol. 232, no. 3, pp. 701-701.

Primack SJ. (2010). A physiatrist's perspective on musculoskeletal ultrasound. *Phys Med Rehabil Clin N Am*, vol. 21, no. 3, pp. 645-650.

Schmid MR, Kissling RO, Curt A, Jaschko G, & Hodler J. (2006). Sympathetic skin response: monitoring of CT-guided lumbar sympathetic blocks. *Radiology*, vol. 241, no. 2, pp. 595-602.

Schueler BA. (2000). The AAPM/RSNA physics tutorial for residents: general overview of fluoroscopic imaging. *Radiographics*, vol. 20, no. 4, pp. 1115-1126.

Sentinel Event Policy and Procedures. The Joint Commission website. http://www.jointcommission.org/assets/1/18/Radiation_Overdose.pdf. Accessed June 21, 2008.

Shahabi S. Radiation safety/protection and health physics. (1999). In: Dowd SB, Tilson ER, eds. *Practical Radiation Protection and Applied Radiobiology*. 2nd ed. pp. 167-196, Saunders, Philadelphia, Pa.

Shellock FA, Crues JV. (2004). MR procedures: biologic effects, safety, and patient care. *Radiology*, vol. 232, no. 3, pp. 635-652.

Shepp LA, Kruskal JB. (1978). Computerized tomography: the new medical x-ray technology. *Am Math Mon*, vol. 85, no. 6, pp. 420-439.

Sites BD, Brull R, Chan VWS, et al. (2007). Artifacts and pitfall errors associated with ultrasound-guided regional anesthesia. Part I: Understanding the basic principles of ultrasound physics and machine operations. *Reg Anesth Pain Med*, vol. 32, no. 5, pp. 412-418.

Sites BD, Chan VW, Neal JM, et al. (2009). The American Society of Regional Anesthesia and Pain Medicine and the European Society of Regional Anaesthesia and Pain Therapy joint committee recommendations for education and training in ultrasound-guided regional anesthesia. *Reg Anesth Pain Med*, vol. 34, no. 1, pp. 40-46.

Smiddy PF, Quinn AD, Freyne PJ, Marsh D, & Murphy JM. (1996). Dose reduction in double contrast barium enema by use of low fluoroscopic current. *Br J Radiol*, vol. 69, no. 825, pp. 852-854.

Sprawls P. AAPM tutorial. (1992). CT image detail and noise. *Radiographics*, vol. 12, no. 5, pp. 1041-1046.

Stam W, Pillay M. (2008). Inspection of lead aprons: a practical rejection model. *Health Phys*, vol. 95, suppl. 2, pp. S133-S136.

Stübig T, Kendoff D, Citak M, et al. (2009). Comparative study of different intraoperative 3-D image intensifiers in orthopedic trauma care. *J Trauma*, vol. 66, no. 3, pp. 821-830.

Thoumas D, Leroi AM, Mauillon J, et al. (1999). Pudendal neuralgia: CT-guided pudendal nerve block technique. *Abdom Imaging*, vol. 24, no. 3, pp. 309-312.

Tuohy B, Marsh DM, O'Reilly G, Dowling A, Cooney P, & Malone JF. (1997). Quality assurance programme applied to mobile C-arm fluoroscopy systems. *Eur Radiol*, vol. 7, no. 4, pp. 534-541.

U.S. Food and Drug Administration Radiation Emitting Products: Radiation Emitting Products and Procedures: Medical Imaging: Ultrasound Imaging: http://www.fda.gov/Radiation-EmittingProducts/RadiationEmittingProductsandProcedures/MedicalImaging/ucm115357.htm. n.d.

U.S. National Academy of Sciences, National Research Council, Committee to Assess Health Risks from Exposure to Low Levels of Ionizing Radiation. Health Risks from Exposure to Low Levels of Ionizing Radiation. BEIR VII Phase 2. Washington, DC: National Academies Press, 2006.

U.S. National Institutes of Health. Safety study of deep brain stimulation to manage thalamic pain syndrome. Identifier: NCT01072656. Clinical Trials website. http://clinicaltrials.gov. Accessed May 16, 2011

U.S. National Institutes of Health. Vercise implantable stimulator for treating Parkinson's disease (VANTAGE). Identifier: NCT01221948. Clinical Trials website. http://clinicaltrials.gov. Accessed May 16, 2011.

Vano E, Gonzalez L, Ten JI, et al. (2001). Skin dose and dose-area product values for interventional cardiology procedures. *Br J Radiol*, vol. 74, no. 877, pp. 48-55.

Villavicencio AT, Burneikiene S, Bulsara KR, & Thramann JJ. (2005). Intraoperative three-dimensional fluoroscopy-based computerized tomography guidance for percutaneous kyphoplasty. *Neurosurg Focus*, vol. 18, no. 3, p. E3.

Wagner AL. (2004a). Selective lumbar nerve root blocks with CT fluoroscopic guidance: technique, results, procedure time, and radiation dose. *AJNR Am J Neuroradiol*, vol. 25, no. 9, pp. 1592-1594.

Wagner AL. (2004b). CT fluoroscopy-guided epidural injections: techniques and results. *AJNR Am J Neuroradiol*, vol. 25, no. 10, pp. 1821-1823.

Wang J, Blackburn TJ. (2000). The AAPM/RSNA physics tutorial for residents: x-ray image intensifiers for fluoroscopy. *Radiographics*, vol. 20, no. 5, pp. 1471-1477.

Whitworth ML. Fluoroscopy scatter radiation studies of the lumbar spine. In: Interventional Spine. Volume 5, Issue 5. Kentfield, Ca: International Spine Intervention Society, n.d.

Wininger KL. (2010). The lumbosacral spine: kinesiology, physical rehabilitation, and interventional pain medicine. *Clinical Kinesiology*, vol. 64, no. 3, pp. 22-50.

Wininger KL, Deshpande KK, & Deshpande KK. (2010). Radiation exposure in percutaneous spinal cord stimulation mapping: a preliminary report. Pain Physician, vol. 13, no. 1, pp. 7-18.

World Health Organization. The WHO Global Database on Body Mass Index. BMI Classification website. http://apps.who.int/bmi/index.jsp?introPage=intro_3.html. n.d.

Yanch JC, Behrman RH, Hendricks MJ, & McCall JH. (2009). Increased radiation dose to overweight and obese patients from radiographic examinations. *Radiology*, 2009, vol. 252, no. 1, pp. 128-139.

Zhou Y, Singh N, Abdi S, Wu J, Crawford J, Furgang FA. (2005). Fluoroscopy radiation safety for spine interventional pain procedures in university teaching hospitals. *Pain Physician*, vol. 8, no. 1, pp. 49-53.

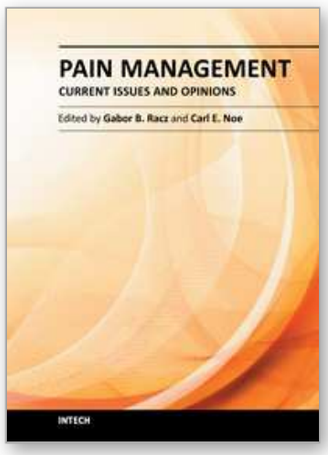

Pain Management - Current Issues and Opinions

Edited by Dr. Gabor Racz

ISBN 978-953-307-813-7
Hard cover, 554 pages
Publisher InTech
Published online 18, January, 2012
Published in print edition January, 2012

Pain Management - Current Issues and Opinions is written by international experts who cover a number of topics about current pain management problems, and gives the reader a glimpse into the future of pain treatment. Several chapters report original research, while others summarize clinical information with specific treatment options. The international mix of authors reflects the "casting of a broad net" to recruit authors on the cutting edge of their area of interest. Pain Management - Current Issues and Opinions is a must read for the up-to-date pain clinician.

How to reference

In order to correctly reference this scholarly work, feel free to copy and paste the following:

Kevin L. Wininger (2012). Applied Radiologic Science in the Treatment of Pain: Interventional Pain Medicine, Pain Management - Current Issues and Opinions, Dr. Gabor Racz (Ed.), ISBN: 978-953-307-813-7, InTech, Available from: http://www.intechopen.com/books/pain-management-current-issues-and-opinions/applied-radiologic-science-in-the-treatment-of-pain-interventional-pain-medicine

INTECH
open science | open minds

InTech Europe
University Campus STeP Ri
Slavka Krautzeka 83/A
51000 Rijeka, Croatia
Phone: +385 (51) 770 447
Fax: +385 (51) 686 166
www.intechopen.com

InTech China
Unit 405, Office Block, Hotel Equatorial Shanghai
No.65, Yan An Road (West), Shanghai, 200040, China
中国上海市延安西路65号上海国际贵都大饭店办公楼405单元
Phone: +86-21-62489820
Fax: +86-21-62489821

IntechOpen